https://doi.org/10.5194/egusphere-2026-2565
Preprint. Discussion started: 20 May 2026
© Author(s) 2026. CC BY 4.0 License.

A robust multi-indicator framework for landslide early warning using complementary statistical physics-based diagnostics

Qinghua Lei[1], Didier Sornette[2]

[1]Department of Earth Sciences, Uppsala University, Uppsala, 752 36, Sweden
[2]Institute of Risk Analysis, Prediction and Management, Academy for Advanced Interdisciplinary Studies, Southern University of Science and Technology, Shenzhen, 518055, China

Correspondence to: Qinghua Lei (qinghua.lei@geo.uu.se) and Didier Sornette (dsornette@ethz.ch)

Abstract. Landslide early warning remains challenging because many slopes evolve through intermittent, nonlinear, and non-monotonic deformation before catastrophic failure. Here, we develop an integrated early warning framework that combines three statistical physics-based diagnostics: velocity b-value tracking, dragon-king detection, and log-periodic power law singularity (LPPLS) time-to-failure analysis. The velocity b-value captures long-term changes in the distribution of slope displacement rates, dragon-king detection identifies statistically significant extreme velocity outliers, and LPPLS analysis describes the quasi-deterministic evolution towards a finite-time singularity yielding probabilistic estimates of the failure time and its uncertainty. Applied pseudo-prospectively to the Preonzo, Veslemannen, and Stampa landslides, the framework reveals a coherent sequence of precursory signals: b-value decline generally appears first, dragon-king outliers emerge later as failure becomes imminent, and LPPLS forecasts become increasingly constrained during the final acceleration stage. These complementary indicators are integrated into a traffic-light warning scheme that translates complex rupture dynamics into operationally interpretable warning levels. By combining precursory signals across multiple timescales, the proposed framework establishes a robust and physically grounded foundation for next-generation landslide early warning.

1 Introduction

Landslides are widespread geohazards that pose severe threats to human life, infrastructure, and economic activity worldwide (Petley, 2012; Froude and Petley, 2018). Their occurrence spans a broad spectrum of processes and scales, ranging from slow movements to catastrophic failures (Lacroix et al., 2020). The increasing exposure of populations due to urbanisation, combined with climate-driven changes such as extreme rainfall and permafrost degradation, is expected to further intensify landslide hazards globally (Gariano and Guzzetti, 2016; Jacquemart et al., 2024). As a result, improving our capability to predict and manage landslide risks has become a central challenge in geohazard mitigation.

In practice, landslide early warning systems are widely implemented to reduce risk, particularly where structural mitigation measures are infeasible. These systems typically rely on monitoring data and predefined thresholds to trigger warnings and evacuations (Krøgli et al., 2018; Michoud et al., 2013). At the regional scale, many early warning systems use rainfall-based

https://doi.org/10.5194/egusphere-2026-2565
Preprint. Discussion started: 20 May 2026
© Author(s) 2026. CC BY 4.0 License.

thresholds or hydrometeorological indicators to estimate landslide hazards (Guzzetti et al., 2007, 2020; Patton et al., 2023; Segoni et al., 2015). At the slope scale, empirical approaches such as velocity thresholds or inverse velocity methods are commonly applied to forecast failure and establish warning levels (Carlà et al., 2017; Crosta et al., 2017; Crosta and Agliardi, 2002, 2003; Intrieri et al., 2012, 2013; Leinauer et al., 2023; Manconi and Giordan, 2015; Segalini et al., 2018). These approaches have proven effective in some cases—for example, the Preonzo landslide, where a velocity threshold-based early warning system enabled timely evacuation prior to catastrophic failure (Loew et al., 2017). However, their applicability becomes limited in more complex settings, such as the Veslemannen landslide (Kristensen et al., 2021), where the system exhibits non-monotonic acceleration behaviour and pronounced intermittency, thereby violating the underlying assumptions of traditional empirical approaches and leading to frequent false alarms.

Recent advances in statistical physics provide a powerful framework for understanding and forecasting catastrophic landslides. From this perspective, landslides approach failure through a finite-time "critical" dynamical instability, where "criticality" is used metaphorically, driven by positive feedback among deformation, damage, weakening, and stress redistribution, with precursory signals (power-law acceleration, log-periodic oscillation, statistical outliers) as its generic signatures (Lei et al., 2023; Lei and Sornette, 2023, 2025b, e). These signatures reflect the underlying heterogeneity and nonlinear dynamics of geological systems, arising from the interplay between endogenous processes (e.g. damage and healing) and exogenous forcing (e.g. rainfall and snowmelt) (Lei and Sornette, 2025a). This perspective opens new opportunities for developing physics-based early warning systems grounded in the fundamental mechanisms of rupture in heterogeneous geomaterials.

In this study, we develop an integrated early warning framework that combines three complementary diagnostics rooted in statistical physics: (1) velocity *b*-value tracking, capturing changes in the distribution of slope displacement rates; (2) dragon-king detection, identifying extreme outliers associated with tertiary creep; and (3) log-periodic power law singularity (LPPLS) analysis, providing probabilistic estimates of time-to-failure. The objective is to demonstrate how combining these indicators can improve the robustness and interpretability of landslide early warning. The remainder of the paper is structured as follows: Section 2 introduces the methodology, Section 3 presents the early warning framework, Section 4 describes the case studies, Section 5 discusses the results and limitations, and Section 6 concludes the paper.

2 Statistical physics-based diagnostic methodology

2.1 Velocity *b*-value tracking

Slope velocities during the pre-failure evolution are generally well described by an inverse gamma distribution (Lei et al., 2023; Lei and Sornette, 2023, 2025a):

$$f(v) = \frac{a^b}{\Gamma(b)} \left(\frac{1}{v-c} \right)^{b+1} \exp\left(-\frac{a}{v-c} \right), \tag{1}$$

https://doi.org/10.5194/egusphere-2026-2565
Preprint. Discussion started: 20 May 2026
© Author(s) 2026. CC BY 4.0 License.

where v is the slope velocity sampled at uniform time intervals (e.g. on a daily basis), $\Gamma(\cdot)$ is the gamma function, $a > 0$ is a scale parameter, $b > 0$ is a shape parameter, and $c < v$ is a constant. The inverse gamma distribution offers a parsimonious formulation that captures the dual nature of slope dynamics, with a power law regime at medium to large velocities arising from short-term intermittent creep, and an exponential rollover with an essential singularity at low velocities associated with long-term background creep (Lei and Sornette, 2023). The inverse gamma distribution exhibits a heavy tail that asymptotically follows a power law, characterised by a tail exponent equal to the shape parameter b. This velocity b-value defines the relative frequency of small to large velocities.

Field observations have shown that catastrophic slope failures are often preceded by a noticeable decline in the velocity b-value, reflecting an increased frequency of larger displacement rates during the acceleration phase (Lei and Sornette, 2025a). Monitoring the temporal evolution of the velocity b-value can thus support the long-term forecasting of catastrophic landslides.

The b-value can be estimated from the time series of slope velocities using a cumulative window approach. For each analysis time, all velocity observations up to that time are collected and fitted with the inverse gamma distribution using the profile likelihood method (Text S1), from which the b-value is obtained. Repeating this procedure sequentially in time yields a continuous trajectory of the b-value, enabling the tracking of its temporal evolution during the pre-failure phase.

2.2 Dragon-king detection

The dragon-king detection method builds on the physics of extreme events in complex natural systems (Sornette and Ouillon, 2012). In the context of landslides, such events correspond to anomalously large velocities that deviate from the background deformation regime as statistical outliers (Lei et al., 2023). Detecting these dragon-kings can therefore provide a short-term diagnostic signal that catastrophic failure may be approaching.

The detection of dragon-kings is performed by applying a statistical test (Lei et al., 2023; Sornette and Wei, 2026) on the ranked slope velocity data $\{v_{(1)} \leq v_{(2)} \leq \ldots \leq v_{(N)}\}$, sorted in ascending order. We define the null hypothesis H_0 that all the velocity data are drawn from the same population (i.e. an inverse gamma distribution), whilst the alternative hypothesis H_1 states that the largest velocities follow a distribution different from that of the smaller velocities.

We first identify outlier candidates based on the Anderson-Darling distance (Malevergne and Sornette, 2006):

$$A^2(\xi) = -n - 2\sum_{i=1}^{n}\left\{\frac{2i}{2n+1}\ln\left[F(v_{(i)})\right] + \left(1 - \frac{2i}{2n+1}\right)\ln\left[1 - F(v_{(i)})\right]\right\}, \tag{2}$$

where $F(\cdot)$ is the cumulative distribution function of the ranked velocity data $\{v_{(1)} \leq v_{(2)} \leq \ldots \leq \xi;\ n \leq N\}$, such that the threshold velocity ξ can be estimated from:

$$\hat{\xi} = \arg\min_{\xi} A^2(\xi; \mathbf{v}), \tag{3}$$

© Author(s) 2026. CC BY 4.0 License.

above which k number of velocities are identified as outlier candidates. We then conduct an outward sequential test, examining increasingly larger outlier candidates $v_{(j)} \in \{v_{(N-k+1)} \leq v_{(N-k+2)} \leq \ldots \leq v_{(N)}\}$ to exclude spurious ones, based on the following test statistic (Lei et al., 2023; Sornette and Wei, 2026):

$$T_{j,k}^{\text{outward}} = \frac{v_{(j)}}{\sum_{i=1}^{N-k} v_{(i)}}. \tag{4}$$

For the remaining r number of outliers $\{v_{(N-r+1)} \leq v_{(N-r+2)} \leq \ldots \leq v_{(N)};\ 0 \leq r \leq k\}$, we conduct a block test using a test statistic defined as (Lei et al., 2023; Sornette and Wei, 2026):

$$T_{r}^{\text{block}} = \frac{\sum_{i=N-r+1}^{N} v_{(i)}}{\sum_{i=1}^{N-r} v_{(i)}}. \tag{5}$$

Monte Carlo simulations (10,000 runs) are conducted to estimate the p-value under the null hypothesis H_0. A systematic decline of the p-value signifies the transition of the slope into the dragon-king regime.

The temporal evolution of the dragon-king p-value is obtained using a cumulative window approach. For each analysis time, all velocity observations up to that time are considered, and the dragon-king detection procedure is applied to the ranked dataset. The corresponding p-value is estimated via Monte Carlo simulations under the null hypothesis. Repeating this procedure sequentially in time yields a p-value time series, which enables tracking of the emergence of dragon-king behaviour.

2.3 LPPLS-based time-to-failure analysis

The time-to-failure analysis in this study is based on the LPPLS model (Sornette and Sammis, 1995; Saleur et al., 1996), which describes accelerating deformation as a finite-time singularity decorated by log-periodic oscillations (see Lei and Sornette, 2025b, c, d, e for recent applications to landslides and other geohazards). The displacement $\Omega(t)$ is expressed as:

$$\Omega(t) = A + \left\{B + C\cos\left[\omega \ln(t_c - t) - \phi\right]\right\}(t_c - t)^m, \text{ with } t < t_c, \tag{6}$$

where t_c is the critical time, m is the critical exponent, ω is the angular log-frequency, ϕ is a phase shift, and A, B, and C are constants. The LPPLS model captures two essential ingredients of rupture dynamics: (i) power-law acceleration driven by positive feedback mechanisms that lead the system towards a finite-time singularity at t_c, and (ii) log-periodic oscillations reflecting the intermittent and hierarchical nature of damage and rupture processes in heterogeneous geomaterials.

The LPPLS model involves seven parameters, with the critical time t_c being the primary quantity of interest. By calibrating the model to time series data, t_c can be estimated and serves as a proxy for the potential failure time. The calibration proceeds as follows. First, a subset of time series is extracted over an interval $[t_0, t_2]$, where t_2 is the current time of analysis and t_0 defines the start of the extraction window. This window is chosen to be sufficiently long to capture potential LPPLS dynamics, but not excessively long so as to compromise computational efficiency. The optimal starting time t_1 (with $t_0 < t_1 < t_2$) of the LPPLS fitting window $[t_1, t_2]$ is then determined using the Lagrange regularisation approach (Demos and Sornette,

© Author(s) 2026. CC BY 4.0 License.

2019). The LPPLS model is subsequently calibrated using the data over [t_1, t_2] to estimate t_c through a stable and robust fitting procedure (Filimonov and Sornette, 2013). Further details of the calibration algorithm are provided in Text S2.

The following parameter filters are applied to enhance the robustness of the fitting: $m < 2$ and $3 < \omega < 15$. For a finite-time singularity to exist, the critical exponent must satisfy $m < 1$. When calibration yields $m > 1$, this indicates that no genuine finite-time singularity is detectable within the current analysis window; in such cases, the fitted t_c does not represent an impending failure but rather marks a forecast horizon beyond which the model loses predictive meaning. Thus, the LPPLS diagnosis remains informative by diagnosing when the observed dynamics fall outside the accelerating regime.

We adopt a probabilistic forecasting framework by constructing a probability density function of t_c. Uncertainty is quantified using a bootstrap approach (Chernick, 2011), in which residuals from the LPPLS fit are resampled to generate multiple synthetic datasets, each used to recalibrate the model and obtain a new t_c estimate. In this study, 20 bootstrap realisations are generated. The resulting ensemble of t_c estimates defines the predictive distribution, which is constructed using adaptive kernel density estimation (Cranmer, 2001). This procedure is applied sequentially as t_2 advances, yielding a time-evolving probability density function of t_c. In addition, a set of diagnostic metrics is derived from the ensemble to assess the stability and reliability of the LPPLS fits (Text S3).

2.4 Complementarity of diagnostic indicators

The three diagnostic approaches—velocity *b*-value tracking, dragon-king detection, and LPPLS time-to-failure analysis—capture complementary aspects of the rupture process across different stages of slope evolution. The velocity *b*-value reflects the transition of the system from secondary to tertiary creep by quantifying the evolving balance between small and large velocities. Dragon-king detection identifies the emergence of extreme behaviour at the final stage, arising from strong positive feedback mechanisms operating during tertiary creep, when damage has become sufficiently mature to organise at the system scale. The LPPLS-based analysis complements these statistical diagnostics by providing a quasi-deterministic description of the temporal evolution towards a finite-time singularity. By characterising the superimposed acceleration-oscillation dynamics, LPPLS augments the *b*-value and dragon-king *p*-value indicators with an explicit time-dependent framework and yields a probabilistic estimate of the critical time together with its associated uncertainty. Taken together, these approaches offer a multi-scale description of the progression of a slope from diffuse deformation to system-scale failure.

3 Integrated early warning framework

3.1 Integration of diagnostic methods

The three diagnostic approaches are integrated within a traffic-light early warning framework. Within this framework, discrete states are defined for the velocity *b*-value, dragon-king *p*-value, and LPPLS indicators (Table 1), reflecting different stages of system evolution and corresponding to increasing levels of destabilisation and proximity to system-scale failure.

For the velocity *b*-value, the states represent a progressive change in the velocity distribution: State 0 corresponds to a stable *b*-value reflecting background velocity fluctuations, State 1 marks the onset of a sustained local reduction in *b*-value, and State 2 indicates a coherent system-wide reduction of *b*-value associated with the growing dominance of large displacement rates. For dragon-king detection, the states represent the progression from the absence of statistically significant extremes (State 0) to first local detection (State 1) and ultimately to coherent detection at the system level (State 2). For LPPLS, the states are defined based on the temporal stability of the predicted critical time t_c distributions and the behaviour of the critical exponent m. State 0 corresponds to scattered and drifting t_c estimates, or to cases where $m \geq 1$, indicating no clear finite-time singularity; State 1 indicates transient clustering of t_c distributions with noisy stabilisation, associated with $m < 1$; State 2 reflects relatively stable clustering of t_c distributions with limited drift and reduced spread, also associated with $m < 1$.

Table 1. Definition of indicator states.

Indicator	State 0	State 1	State 2
Velocity *b*-value	Normal fluctuation: no sustained *b*-value decline across all sensors, or any previous decline has ceased	Local decline: at least one reliable sensor within the active region shows sustained *b*-value decline	Coherent decline: a sustained *b*-value decline is observed across a substantial proportion (e.g. ≥50%) of reliable sensors within the active region
Dragon-king *p*-value	No decline: No apparent *p*-value decline across all sensors	Local decline: at least one reliable sensor shows significant *p*-value decline	Coherent decline: a significant *p*-value decline is observed across a substantial proportion (e.g. ≥50%) of reliable sensors within the active region
LPPLS	No clear LPPLS regime: no stable LPPLS fits, with the t_c distributions scattered and drifting with t_2, or $m \geq 1$	Possible LPPLS regime: transient clustering of t_c distributions across multiple updates, but still drifting and noisy, and $m < 1$	Constrained LPPLS regime: sustained clustering of t_c distributions across multiple updates, with limited drift and moderate spread, and $m < 1$

3.2 Traffic-light early warning system

The diagnostic indicators are integrated within a traffic-light early warning framework that reflects the progressive evolution of slope instability. Rather than combining the indicators through a simple additive score, which would obscure their distinct diagnostic roles, a staged integration approach is adopted. Here, the velocity *b*-value provides early evidence of regime transition, dragon-king detection identifies the onset and subsequent systematisation of extreme behaviour during the final

https://doi.org/10.5194/egusphere-2026-2565
Preprint. Discussion started: 20 May 2026
© Author(s) 2026. CC BY 4.0 License.

stage, and the LPPLS analysis provides additional diagnostic information related to the system's evolution towards a finite-time singularity.

The operational definition of the warning levels is summarised in Table 2. The warning levels are defined using a traffic-light scheme (green–yellow–orange–red), with escalation governed primarily by the sequential behaviour of the *b*-value and dragon-king *p*-value indicators that exhibit more well-defined transitions. The LPPLS states are integrated within the framework to support and reinforce the interpretation of warning levels, but are not used as standalone triggers for escalation. Yellow corresponds to the onset of sustained destabilisation, as indicated mainly by a systematically declining *b*-value. As this signal may be temporary, the yellow level is reversible if the *b*-value stabilises and returns to baseline behaviour in the absence of supporting evidence from other indicators. Orange is issued when the first reliable dragon-king detection appears, signalling that extreme behaviour has emerged locally. Red is issued when dragon-king detections become coherent across a substantial proportion of reliable sensors within the active region over a short time window, indicating that extreme dynamics have developed at the system scale and that failure is likely to be imminent.

In this framework, LPPLS states contribute to the assessment by supporting and reinforcing warning transitions when consistent with the velocity *b*-value and dragon-king *p*-value indicators. The emergence of transient clustering (State 1) and relatively stable clustering (State 2) of t_c distributions provides additional evidence of increasing slope instability and proximity to failure. LPPLS State 0 is typically associated with the green level, States 0–1 with the yellow to orange levels, and State 1–2 with the red level. This complementary role acknowledges the greater sensitivity of LPPLS results to data quality, noise, and fitting procedures.

While the framework does not prescribe specific actions, the warning levels are intended to support decision-making by indicating progressively increasing levels of concern, ranging from routine monitoring (green), through enhanced surveillance (yellow), to preparedness (orange), and immediate response considerations (red), depending on site-specific risk management protocols.

Table 2. Traffic-light early warning system.

Warning level	Velocity *b*-value	Dragon-king *p*-value	LPPLS	Interpretation
Green	State 0–1	State 0	State 0	Stable or recovered creep regime; no clear evidence of ongoing destabilisation
Yellow	State 2	State 0	State 0–1	Early destabilisation; possible transition from secondary to tertiary creep
Orange	State 1–2	State 1	State 0–1	Advanced instability; extreme behaviour has emerged at least locally
Red	State 1–2	State 2	State 1–2	Imminent failure likely; extreme behaviour has become coherent at the system scale

4 Case studies

We apply the proposed traffic-light early warning system to three well-documented and closely monitored historical landslide events: the Preonzo landslide in Switzerland, the Veslemannen landslide in Norway, and the Stampa rockfall in Norway. The analysis is conducted in a pseudo-prospective manner, whereby the "current" time is progressively advanced towards failure, and all diagnostics are evaluated using only the data available up to each given current time, thereby minimising hindsight bias.

4.1 Preonzo landslide, Switzerland

The Preonzo landslide is a large rock slope instability located above the village of Preonzo in the Canton of Ticino, southern Switzerland. The instability complex is composed mainly of amphibolite gneiss, augen gneiss, and biotite-rich gneiss (Gschwind et al., 2019). Owing to the exposure of critical infrastructure at the slope toe, including industrial facilities and transportation routes, a long-term monitoring campaign was implemented (Loew et al., 2017). This included five extensometers (with a measurement accuracy of at least 0.01 mm) installed in 1999 to measure the opening of tension cracks in the headscarp area, and a robotic total station installed in 2010 at the valley floor to measure slope surface displacements via multiple reflectors (with a measurement accuracy of about 0.6 mm). An operational early warning system based on velocity thresholds was implemented, enabling the definition of pre-alarm, alarm, and evacuation levels (Loew et al., 2017). A catastrophic failure occurred on 15 May 2012, releasing approximately 210,000 m^3 of rock. Here, we revisit this failure event using our proposed traffic-light early warning framework.

Figure 1 shows the temporal evolution of slope displacement and daily velocity recorded by extensometers and reflectors for the Preonzo landslide. The displacement time series exhibit a prolonged period of relatively slow and steady movement, followed by a pronounced acceleration phase approaching failure, reflecting a transition from secondary to tertiary creep. The corresponding velocity time series are characterized by intermittent fluctuations with occasional bursts, but display a clear and systematic increase in the weeks preceding the collapse. The inset panels (Fig. 1, right) highlight this late-stage acceleration, where velocities rapidly escalate, indicating the emergence of an instability process at the slope scale.

Figure 2 shows the evolution of the probability density functions of slope velocities for both extensometers and reflectors at selected times during the pre-failure phase. The empirical velocity distributions are presented together with inverse gamma fits. As the system approaches failure, the fitted b-value progressively decreases, reflecting an increasing contribution of larger velocities relative to smaller ones. In the final stage (over the last ten days), some extreme velocities appear that deviate from the inverse gamma distribution, suggesting the emergence of anomalous deformation activity preceding the final catastrophic failure.

We further show the temporal evolution of the velocity b-value and the dragon-king p-value, computed on a daily basis, for both extensometers and reflectors (Fig. 3). From mid-March, extensometer E3 starts to exhibit a decline in the b-value, followed shortly by E1 and E2, whereas E4 and E5 only show a noticeable decrease from early May (Fig. 3a, left). A systematic b-value decline is also evident in the reflector data, initiating with R2, R4, and R5 from mid-April and followed by R8 and R9 from late April (Fig. 3b, left). This progressive decrease in b-value across sensors signifies the gradual destabilisation of the slope. The temporal derivative of the b-value (Fig. S1) further highlights this transition, showing a clear shift towards increasingly negative rates of change as failure approaches.

In parallel, the p-value remains at unity for most of the observation period (Fig. 3, right), suggesting that the velocity data are generally well described by the inverse gamma distribution. However, over the last two weeks before failure, the p-value drops abruptly to low values, with different sensors responding at slightly different times. The earliest p-value decline is observed in the reflector data from 2 May, followed by a rapid and systematic decrease across all sensors. This systematic decline in p-value signals a statistically significant deviation from the background inverse gamma distribution, reflecting the emergence of velocity outliers and the imminence of catastrophic failure.

We then show the time-to-failure analysis based on the LPPLS model (see Fig. 4 for the results based on extensometer E1 and reflector R2, and see Fig. S2 for other sensors). The left panels show that the LPPLS fits progressively improve as the system approaches failure. At earlier stages (in late April), the model provides limited constraint on the failure time t_c, resulting in broad probability density functions. As failure approaches and more data recording the accelerating dynamics become available, the LPPLS model increasingly captures both the accelerating trend and the superimposed oscillatory behaviour of the displacement time series, leading to progressively sharper and more concentrated t_c distributions. On the last day before failure (14 May), the probability density function becomes highly peaked around the actual failure time, with a substantial reduction in uncertainty. The right panels show the temporal evolution of the predictive distribution of t_c. At early times, the predicted t_c values exhibit strong fluctuations and are sometimes widely scattered, reflecting large variability. With time, the predictions become relatively stabilised, and the associated uncertainty generally decreases, particularly in the final day before failure. However, this stabilisation remains transient and limited, with the predicted t_c distributions exhibiting noticeable fluctuations rather than persistent convergence. Additional diagnostic metrics of the LPPLS fits show a tendency towards reduced uncertainty and transient clustering as failure is approached, while the critical exponent m evolves towards values below 1 since early March 2012 (Fig. S3).

Figure 5 summarises the temporal evolution of the velocity b-value state, the dragon-king p-value state, the LPPLS state, and the resulting warning level. The b-value transitions from State 0 to State 1 in late March, after observing a sustained decline in at least one sensor, and further to State 2 in mid-April, when a majority of sensors exhibit sustained declines. The dragon-king detection remains in State 0 until early May, then shifts to State 1 on 3 May and to State 2 on 9 May. The LPPLS state remains at State 0 for most of the observation period and transitions to State 1 from 5 May, indicating a brief and noisy clustering of the t_c distributions in the final stage prior to failure. Based on these transitions, the warning level changes from green to yellow on 20 April, remains orange until early May, and then escalates to orange on 3 May and to red on 9 May, persisting until the failure on 15 May.

(a) Extensometers

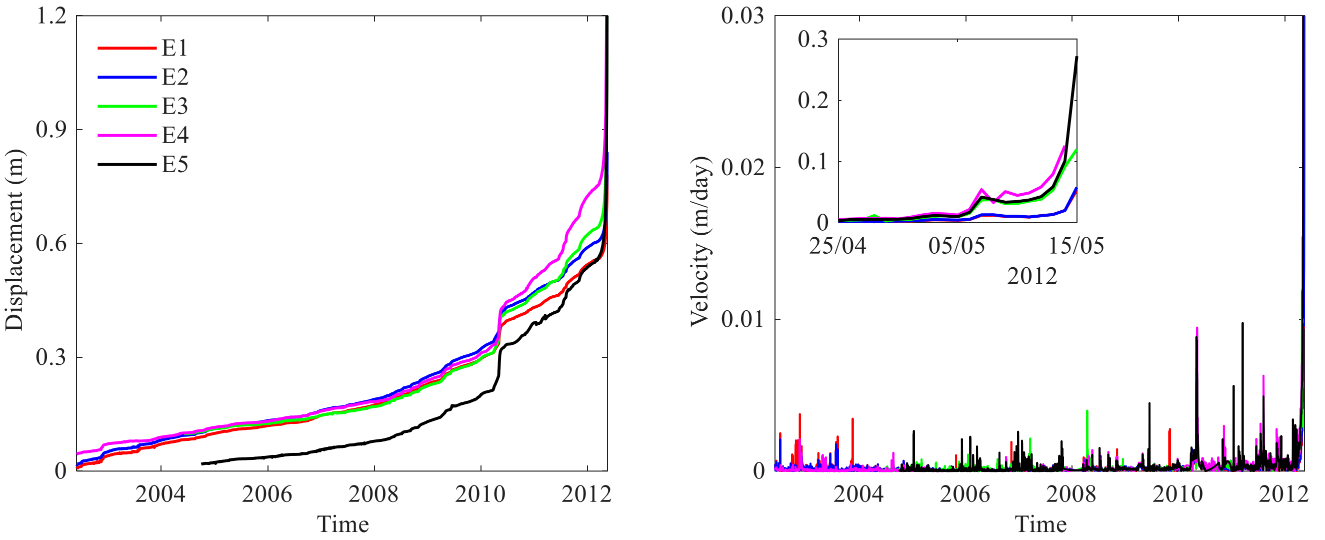

(b) Reflectors

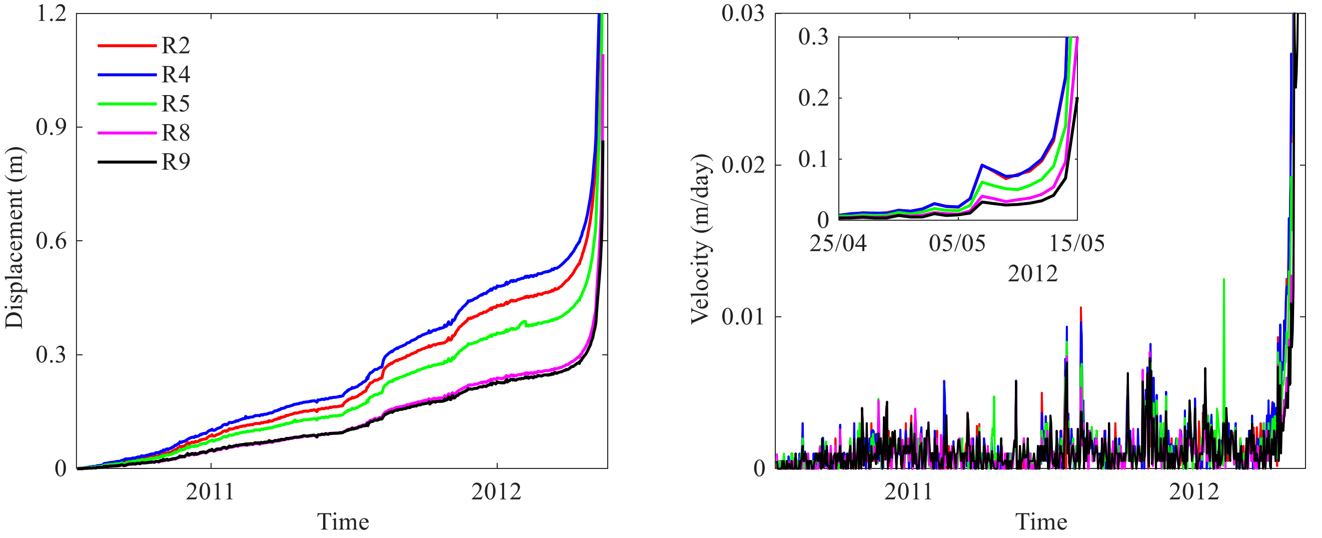

Figure 1: Time series of slope displacement and daily velocity of the Preonzo landslide, measured by (a) five extensometers (E1–E5) and (b) five reflectors (R2, R4, R5, R8, and R9).

https://doi.org/10.5194/egusphere-2026-2565
Preprint. Discussion started: 20 May 2026
© Author(s) 2026. CC BY 4.0 License.

(a) Extensometers

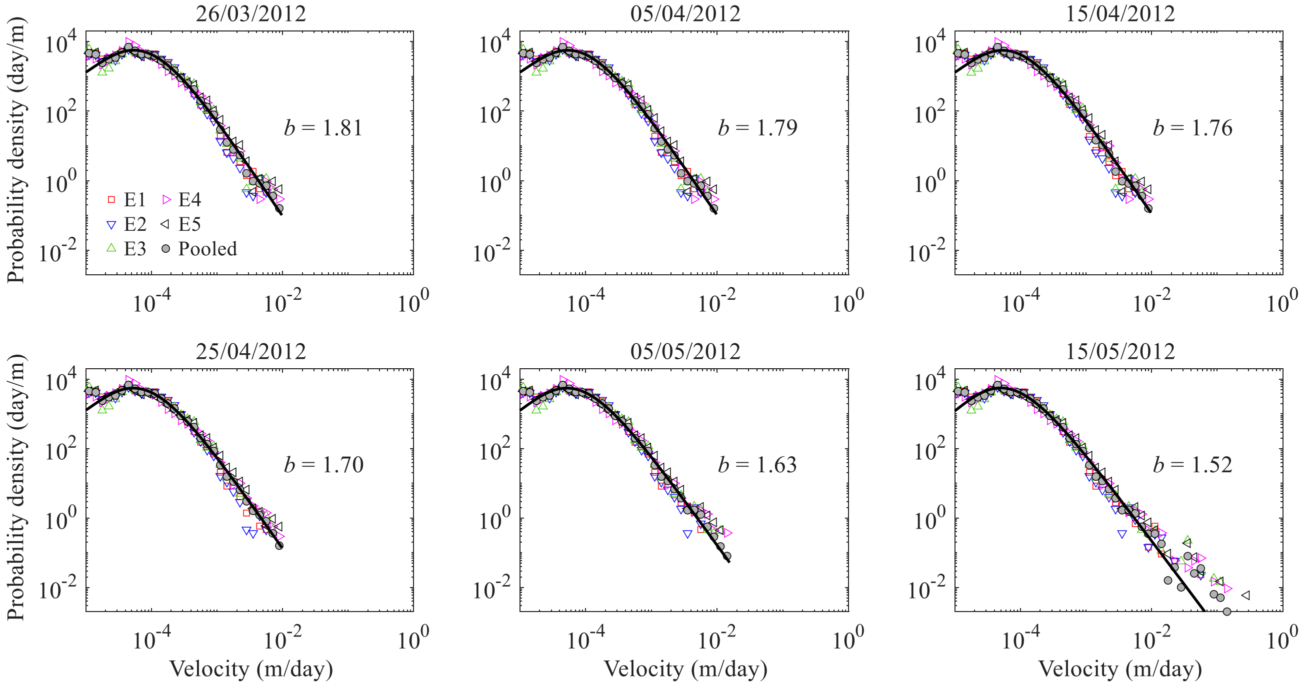

(b) Reflectors

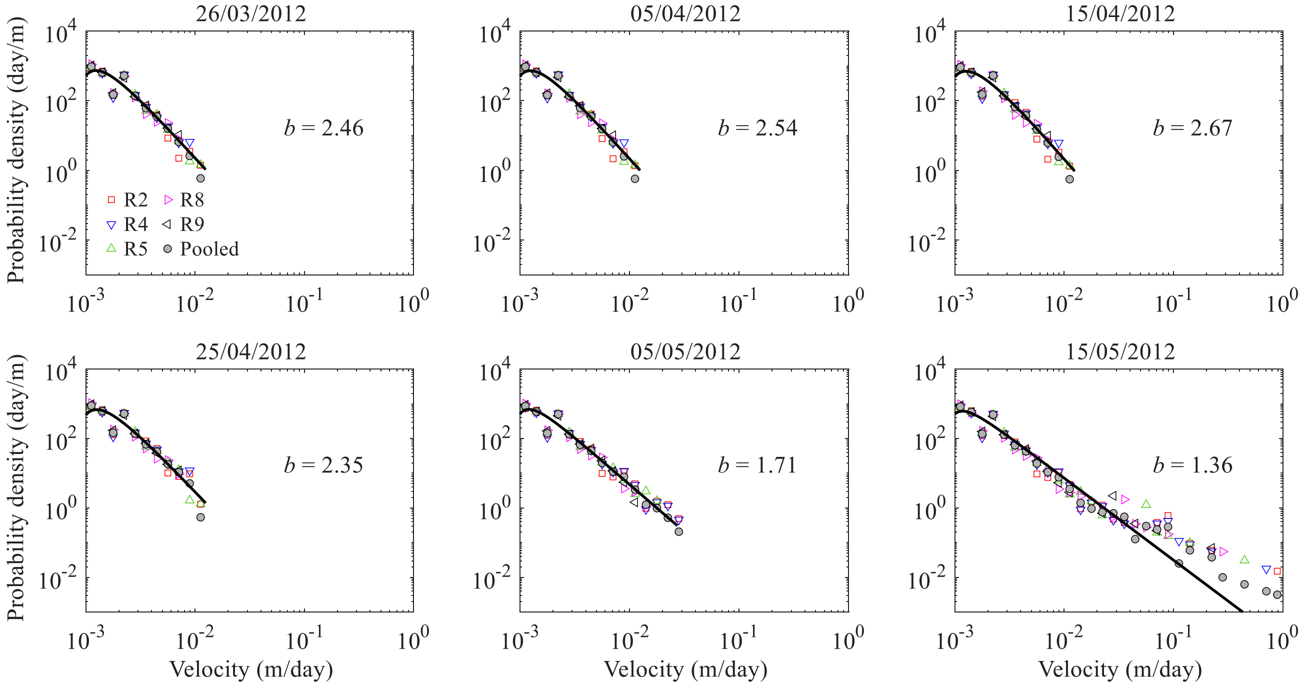

Figure 2: Probability density distributions of slope velocity at different stages of the Preonzo landslide, derived from (a) extensometers and (b) reflectors. Markers represent empirical data and solid curves show the fitted inverse gamma distribution to the pooled data, with the tail exponent *b* indicated.

https://doi.org/10.5194/egusphere-2026-2565
Preprint. Discussion started: 20 May 2026
© Author(s) 2026. CC BY 4.0 License.

(a) Extensometers

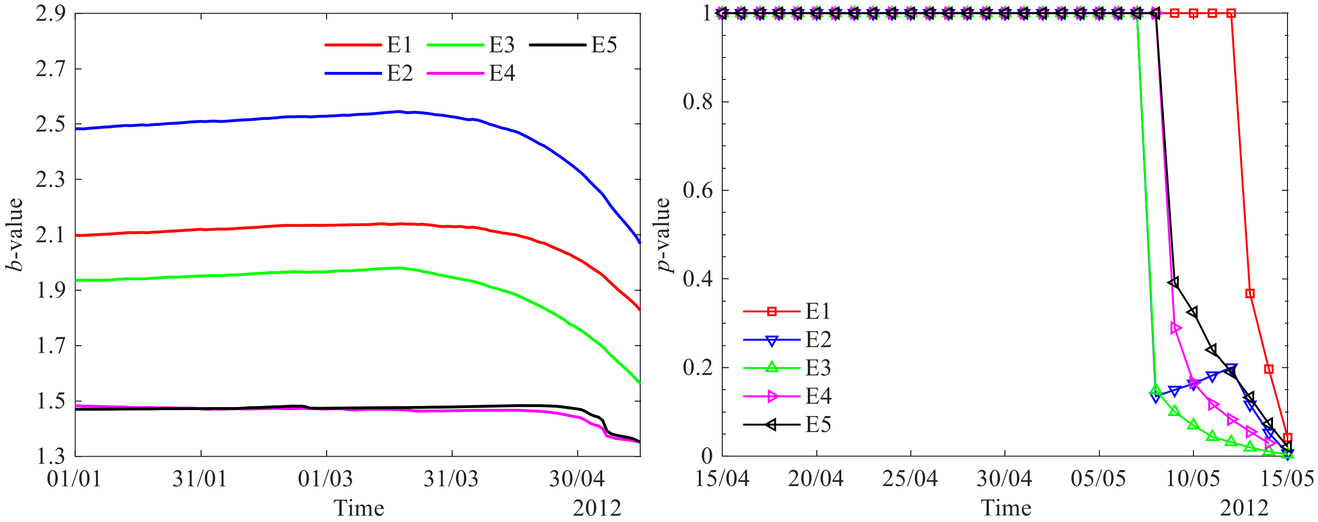

(b) Reflectors

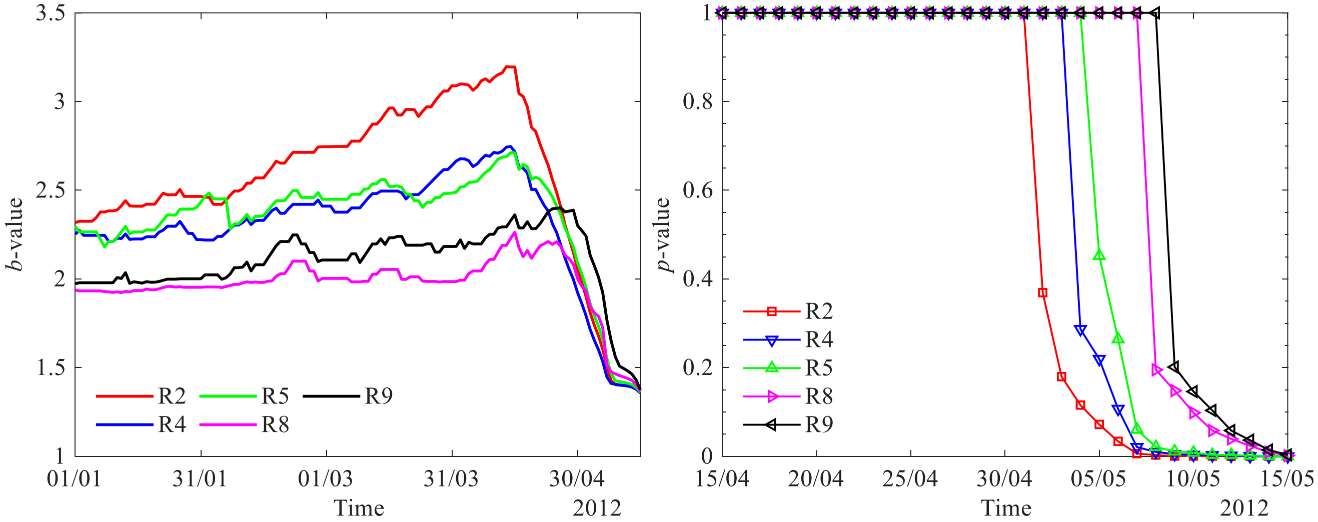

Figure 3: Temporal evolution of the velocity *b*-value (left) and dragon-king *p*-value (right) of the Preonzo landslide, computed on a daily basis using data of individual (a) extensometers and (b) reflectors.

https://doi.org/10.5194/egusphere-2026-2565
Preprint. Discussion started: 20 May 2026
© Author(s) 2026. CC BY 4.0 License.

(a) Extensometer E1

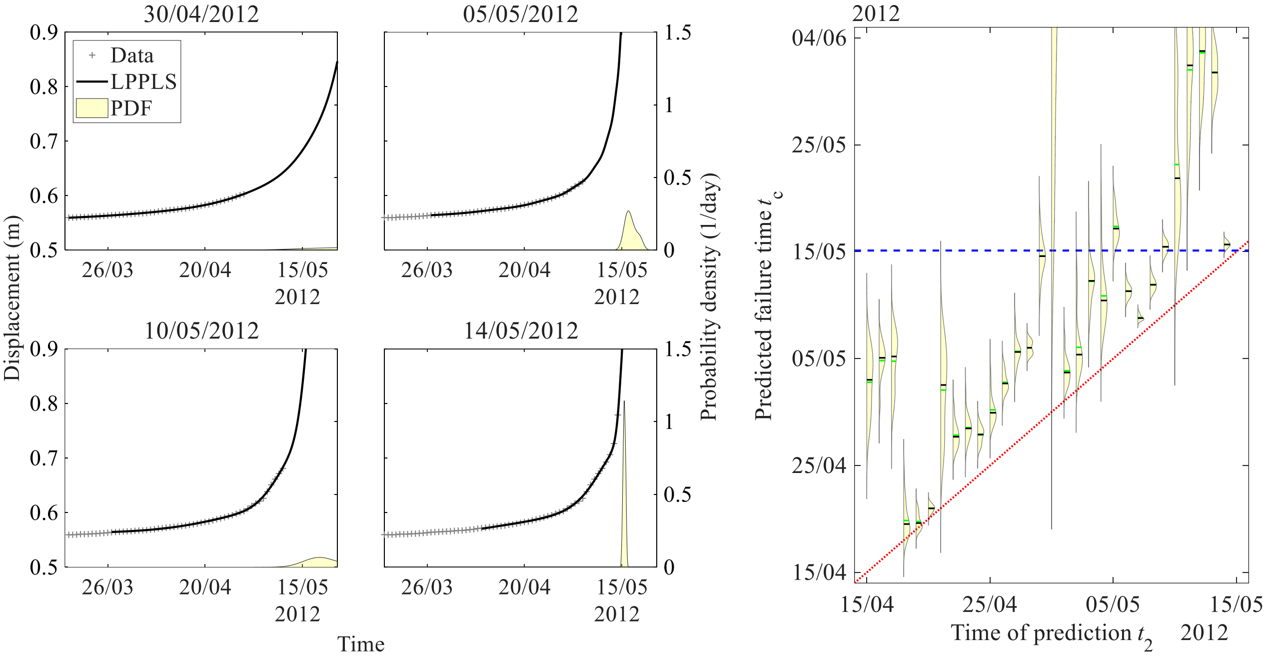

(b) Reflector R2

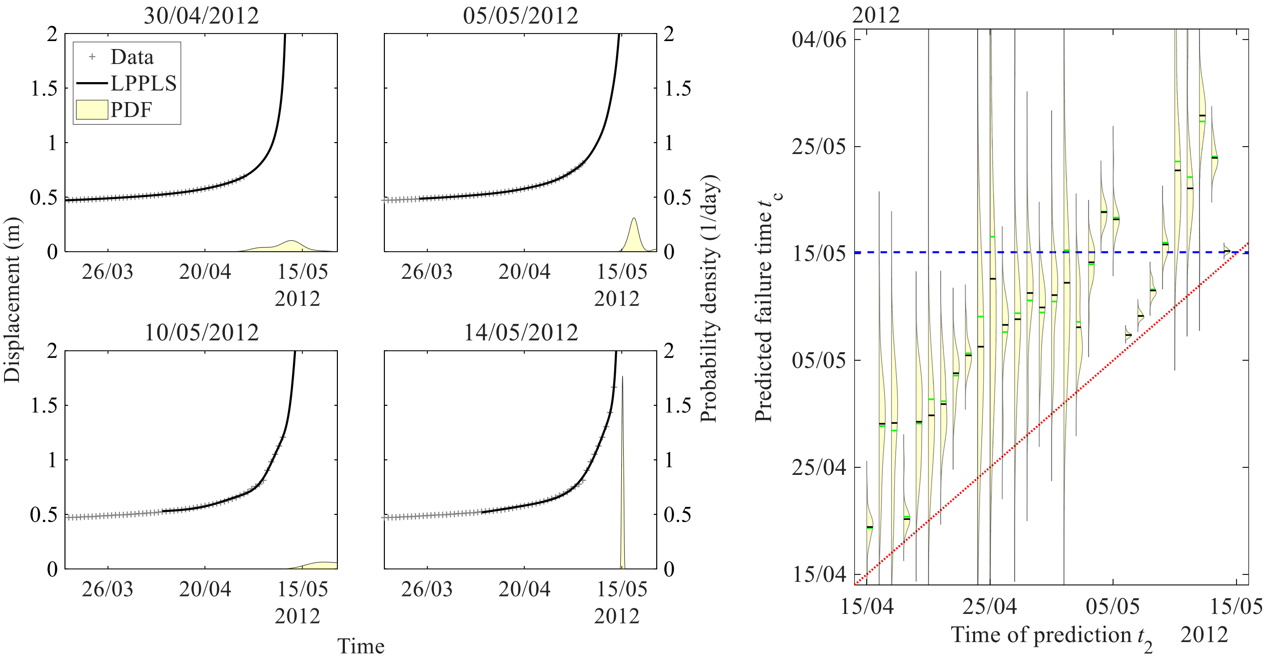

Figure 4: LPPLS-based time-to-failure analysis for the Preonzo landslide based on (a) extensometer E1 and (b) reflector R1. Left panels show the LPPLS fits to displacement data at selected times (15, 10, 5, and 1 days before failure) and the corresponding probability density functions (PDFs) of t_c. Right panels show the PDF evolution of anticipated failure time t_c as a function of analysis time t_2. The green and black lines within each violin indicate the mean and median of the predicted t_c distribution. The red dotted line indicates the reference line $t_c = t_2$, while the blue dashed line marks the observed failure time (15 May 2012, 02:45).

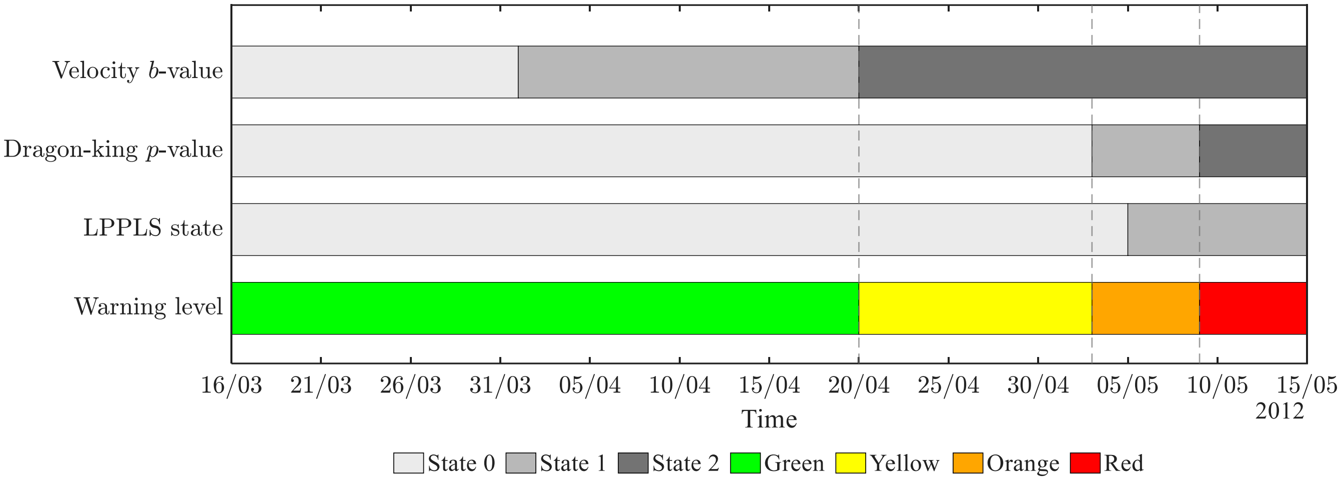

Figure 5: Temporal evolution of indicator states of velocity *b*-value, dragon-king *p*-value, and LPPLS, and the resulting traffic-light warning level, for the Preonzo landslide.

4.2 Veslemannen landslide, Norway

The Veslemannen landslide is located in Romsdalen, western Norway, and forms part of a larger deep-seated gravitational slope deformation developed in high-grade metamorphic rocks influenced by seasonal frost and permafrost conditions (Magnin et al., 2019). The unstable rock mass exhibits episodic movements, primarily during late summer and autumn, associated with thawing and hydrological forcing (Kristensen et al., 2021). Owing to the high risk posed to nearby infrastructure, a comprehensive monitoring system was implemented, including a ground-based interferometric radar installed at the valley floor to provide continuous, high-resolution measurements of surface displacement across the unstable slope (Kristensen et al., 2021). The Norwegian Water Resources and Energy Directorate operates an early warning system based on a colour-coded hazard scheme (green–yellow–orange–red), in which warning levels are defined using velocity thresholds and expert assessment (Krøgli et al., 2018). In total, 16 red alarms were issued between 2014 and 2019 prior to the failure, leading to repeated evacuations of the risk zone; the slope failed only after the last red alarm, whereas no collapse occurred during the preceding 15 alarms despite evacuations (Kristensen et al., 2021). The final catastrophic failure occurred on 5 September 2019, following a period of accelerated deformation. In this study, we revisit the monitoring data using our proposed traffic-light early warning system integrating multiple diagnostic indicators.

Figure 6a shows the temporal evolution of slope displacement and daily velocity recorded by seven radar points for the Veslemannen landslide. The displacement time series exhibit episodic step-like increases superimposed on a long-term accelerating trend, reflecting repeated phases of activation and partial stabilisation. The corresponding velocity time series are characterised by intermittent bursts, with background activity punctuated by short-lived high-velocity events. In the final stage prior to failure, the velocity time series tends to exhibit more persistent episodes of elevated activity (as highlighted in the inset of Fig. 6a, right), suggesting a transition towards a more unstable regime.

https://doi.org/10.5194/egusphere-2026-2565
Preprint. Discussion started: 20 May 2026
© Author(s) 2026. CC BY 4.0 License.

Figure 6b shows the evolution of the probability density functions of slope velocities at selected times during the pre-failure phase. The empirical data are well described by the inverse gamma distribution across different stages of the landslide evolution. At earlier stages, relatively high *b*-values indicate the dominance of small velocities associated with background creep deformation. Although large velocities are observed, particularly in 2018, they largely follow the same inverse gamma distribution as smaller velocities. As the system approaches failure, the *b*-value decreases progressively, from values of about 2.2–2.3 in 2017 to around 1.7–1.8 in 2018, and further to approximately 1.3–1.4 in 2019, reflecting an increasing contribution of medium-to-large velocities.

Figure 6c shows the temporal evolution of the velocity *b*-value and the dragon-king *p*-value, computed on a daily basis, for all radar points. The *b*-value exhibits a staged decline throughout the pre-failure period. A significant and coherent decrease across all radar points is observed in late 2018, followed by a period of relative stabilisation. A renewed decline emerges from July 2019, and a further coherent decrease across multiple radar points develops during the final two weeks prior to failure. This multi-stage evolution is consistent across the radar points and is further highlighted by the temporal derivative of the *b*-value (see Fig. S4), which shows corresponding episodes of negative rates of change. The dragon-king *p*-value remains at unity prior to mid-2018, suggesting that the velocity data are well described by the inverse gamma distribution. From September to November 2018, only a few radar points show temporary decreases in *p*-value, while most radar points do not exhibit a clear response. A more systematic decline emerges from mid-August 2019, when multiple radar points display decreasing *p*-values. On 2 September 2019, all individual *p*-values drop substantially, marking a coherent deviation from the background deformational behaviour across the slope. This temporal evolution indicates that statistically significant anomalies only become widespread shortly before failure.

We further present the time-to-failure analysis based on the LPPLS model (see Fig. 7 for the results based on radar point P2, and see Fig. S5 for other radar points). Figure 7a illustrates the progressive emergence of the LPPLS structure as failure is approached during the 2019 acceleration event. At early stages (in July 2019), only limited data are available and the displacement evolution is weakly constrained, resulting in poorly defined LPPLS fits and broad probability density functions of the predicted failure time t_c. As more data capturing the accelerating and intermittent deformation become available (particularly from mid-August onwards), the LPPLS model becomes increasingly constrained, progressively being “locked” onto the underlying temporal structure of the displacement time series. This leads to improved fits and more concentrated t_c distributions. In the final stage prior to failure, the LPPLS formulation captures both the accelerating trend and the superimposed intermittent behaviour, resulting in a well-constrained prediction of the failure time.

Figure 7b shows the temporal evolution of the predictive distribution of t_c as the analysis time t_2 advances during the final two months before failure. At early times, the predicted t_c values exhibit strong fluctuations and are widely scattered with pronounced variability. With time, the predictions become intermittently more clustered, although noticeable drifting and fluctuations persist, indicating partial or transient stabilisation of the t_c distributions. Only in the final weeks prior to failure do the predicted t_c values cluster closer to the observed failure time and become more sustained, accompanied by a narrower spread. Results from other radar points (Fig. S5) show a broadly consistent behaviour, with high variability and significant drifting at early stages, while the associated uncertainty is gradually reduced on the approach to failure. Additional diagnostic metrics further illustrate this behaviour (Fig. S6): large variability is observed at earlier stages, followed by a general reduction in uncertainty towards failure, while the critical exponent m remains below 1 with reduced variability prior to failure, indicating that the LPPLS fits become increasingly well constrained.

Figure 8 summarises the temporal evolution of the velocity b-value state, the dragon-king p-value state, the LPPLS state, and the resulting warning level for the Veslemannen landslide. The b-value transitions from State 0 to State 1 in late summer 2018 and further to State 2 in early autumn 2018, followed by a return to State 1 and subsequently to State 0 during late autumn and winter 2018–2019. A renewed transition occurs from July 2019, with the b-value reaching State 2 again in the final stage prior to failure. The dragon-king p-value remains in State 0 for most of the observation period, with intermittent and localised transitions to higher states in autumn 2018 that are short-lived and not spatially coherent across sensors. A sustained and system-wide transition to State 2 only emerges from mid-August 2019 onwards. The LPPLS state remains predominantly at State 0 throughout 2018 and for most of early 2019. During autumn 2018, it exhibits brief and fragmented transitions between States 1 and 2, which are not sustained. It shows intermittent transitions to State 1 and brief, non-sustained excursions to State 2 around May 2019, before reverting to lower states. From mid-July 2019, State 1 becomes more persistent, although a brief return to State 0 occurs in early August, followed by a renewed transition to State 1 in mid-August. A sustained transition to State 2 then emerges from late August 2019 onwards in the final stage prior to failure. Based on these transitions, the warning level evolves from green to yellow and then switches intermittently between yellow and orange during autumn 2018, followed by a brief return to green. Thereafter, it remains predominantly at orange from November 2018 until mid-August 2019. Finally, the warning level escalates to red about three weeks before failure.

https://doi.org/10.5194/egusphere-2026-2565
Preprint. Discussion started: 20 May 2026
© Author(s) 2026. CC BY 4.0 License.

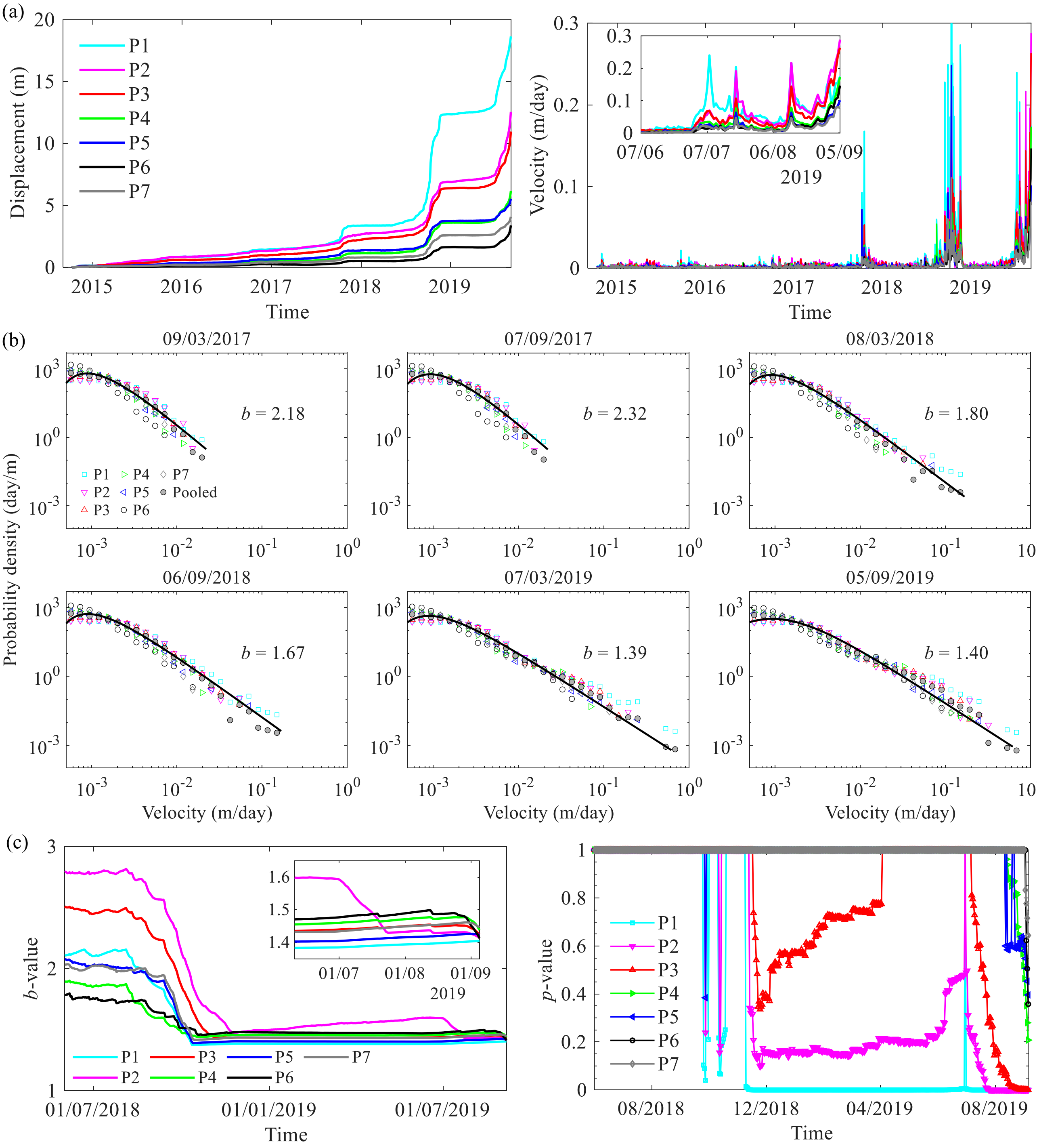

Figure 6: (a) Time series of displacement and daily velocity of the Veslemannen landslide, measured by seven radar points (P1–P7). (b) Probability density distributions of slope velocity at selected dates, with fitted inverse gamma distributions to the pooled data and corresponding tail exponent *b* indicated. (c) Temporal evolution of the velocity *b*-value (left) and dragon-king *p*-value (right) computed on a daily basis using data of individual radar points.

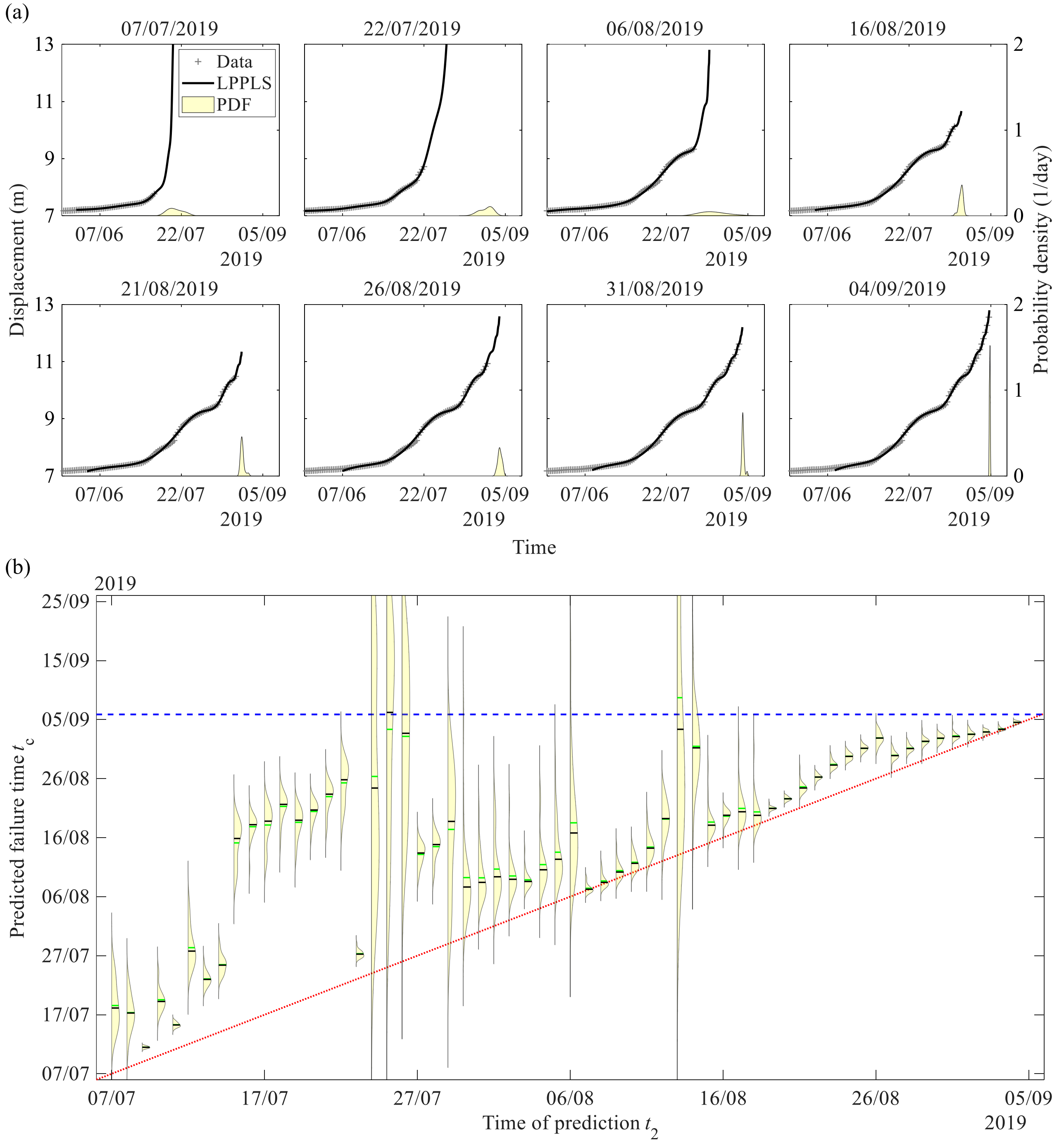

Figure 7: LPPLS-based time-to-failure analysis for the Veslemannen landslide based on radar point P2. (a) LPPLS fits to displacement data at selected times (60, 45, 30, 15, 10, 5, and 1 days before failure) and the corresponding probability density functions (PDFs) of t_c. (b) Evolution of the PDF of anticipated failure time t_c as a function of analysis time t_2. The green and black lines within each violin indicate the mean and median of the predicted t_c distribution. The red dotted line indicates the reference line $t_c = t_2$, while the blue dashed line marks the observed failure time (05 September 2019, 20:58). 355

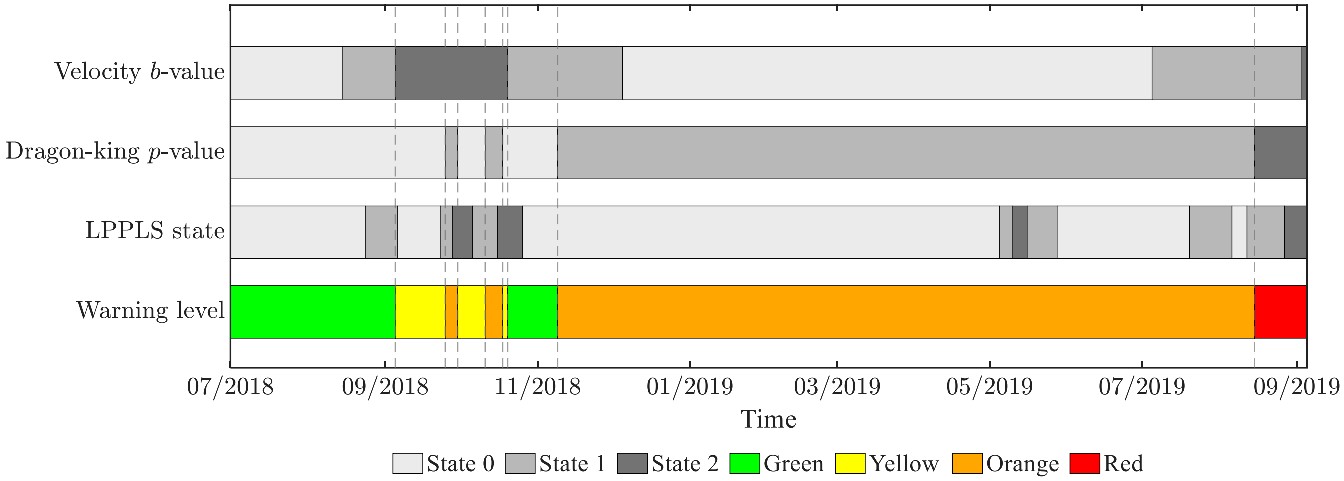

Figure 8: Temporal evolution of indicator states of velocity *b*-value, dragon-king *p*-value, and LPPLS, and the resulting traffic-light warning level, for the Veslemannen landslide.

4.3 Stampa landslide, Norway

The Stampa rock slope in western Norway is a large, unstable rock mass located above the Aurlandsfjord near the village of Flåm, directly overlooking the highly trafficked E16 highway. An unstable sector consisting of about 5,400 m^3 rock within a northwest-facing slope has exhibited progressive deformation over years prior to a catastrophic failure in early July 2023 (Maschler et al., 2026). The failure occurred as a multistage event with two main collapses on 1 July and 3 July 2023. The initial failure involved the unstable basal part of approximately 12,200 m^3, followed by the collapse of the remaining upper rock mass of around 41,800 m^3 (Maschler et al., 2026). The slope has been monitored using a multi-sensor network, including ground-based radar, total station, extensometers, tiltmeters, and satellite observations (Maschler et al., 2026; Schild et al., 2023). In operational practice, early warning is based on continuous monitoring of displacement and velocity, combined with expert assessment of evolving slope conditions (Maschler et al., 2026). In this study, we focus on the ground-based interferometric synthetic-aperture radar data to examine our proposed traffic-light early warning system.

Figure 9a shows the temporal evolution of slope displacement and daily velocity recorded by the radar points. The displacement time series exhibit a long period of progressive deformation from 2017 to 2022, characterised by relatively slow and steady movement. A clear acceleration phase emerges during 2022, followed by a pronounced acceleration in 2023 leading up to the failure events (Fig. 9a, left). The corresponding velocity time series are characterised by low-amplitude fluctuations during most of the monitoring period, but show distinct spikes in 2022 and pronounced bursts in 2023 associated with the final failure phase (Fig. 9a, right). The inset (Fig. 9a, right) highlights this last stage, where velocities increase rapidly in the days immediately preceding failure.

Figure 9b presents the evolution of the probability density functions of slope velocities at selected times, computed from data aggregated over 4-hour intervals. This higher temporal resolution is adopted for the Stampa case to capture the rapid evolution of deformation dynamics preceding failure. The empirical velocity distributions are shown together with inverse gamma fits. At earlier stages (e.g. in 2022), the distributions are well described by the inverse gamma model with relatively high *b*-values (around 2.5–2.6), indicating the dominance of small velocities. As the system approaches failure in 2023, the *b*-value decreases progressively to ~1.9, reflecting an increasing contribution of larger velocities. In the final stage, some deviations from the inverse gamma distribution appear at large velocities, suggesting the emergence of anomalous deformation activity on the approach to failure.

Figure 9c shows the temporal evolution of the velocity *b*-value and the dragon-king *p*-value, computed using 4-hour intervals, for all radar points. The *b*-value remains relatively high and stable during most of 2022, before showing a clear and coherent decline in late 2022 across all radar points. This transition is further highlighted in Fig. S7, where the time derivative of the *b*-value exhibits a pronounced negative excursion during this period. After a period of relative stabilisation at lower values, a second decline emerges from mid-June 2023 and intensifies into a pronounced and coherent decrease across all radar points in late June, immediately preceding failure, again reflected by strong negative peaks in the *b*-value derivative (Fig. S7). In parallel, the *p*-value remains at unity for most of the observation period, indicating that the velocity data are generally consistent with the inverse gamma distribution. Starting from late June 2023, however, the *p*-value drops abruptly across all radar points, with the earliest decreases observed at P3, P13, and P14 on 30 June, followed by the remaining points on 1 July.

Figure 10 shows the LPPLS time-to-failure analysis results using data from radar point P3, located at the basal part of the slope that collapsed during the first failure event on 1 July 2023. Figure 10a shows that the LPPLS fits progressively capture the accelerating displacement trend over the short analysis window. At early stages (e.g. on 28–29 June), the fits are weakly constrained. Although the corresponding probability density functions of the predicted failure time t_c can appear sharp at certain times, they are often centred very close to the analysis time t_2, indicating a clear drifting behaviour. As additional data capturing the rapid acceleration become available, particularly from 30 June onwards, the LPPLS fits become increasingly constrained and the associated t_c distributions shift away from t_2. In the final stage prior to failure, the model captures the pronounced acceleration of the basal deformation, leading to a concentrated predictive distribution around the failure time of the first event. Figure 10b shows the temporal evolution of the predictive distribution of t_c. At early times (before 28 June), the predicted t_c values are widely scattered with large variability. From around 28–29 June, the predictions exhibit a transient plateau, followed by a second plateau from 29 to 30 June, indicating periods of relatively stable prediction performance. From 30 June onwards, the predictions become progressively more stabilised and begin to cluster around the observed failure time. In the final day prior to failure, the predicted t_c lies close to 1 July, with reduced uncertainty.

Figure 11 shows the LPPLS-based time-to-failure analysis for the second failure event using data from radar point P12, which is located in the upper part of the slope that collapsed during the second event on 3 July 2023. Figure 11a illustrates that the LPPLS fits continue to capture the accelerating displacement trend as the system evolves towards the second failure following the first event. In late June, the predicted t_c distributions exhibit large variability but already show an early stabilisation, forming a rough plateau around 30 June to 1 July that corresponds closely to the timing of the first failure

© Author(s) 2026. CC BY 4.0 License.

event. As new data capturing the continued acceleration dynamics become available from 1–2 July, the LPPLS fits progressively stabilise further and begin to reflect the evolving deformation more reliably. In the final stage prior to the second failure, the model captures the rapid acceleration of the remaining unstable mass, leading to concentrated t_c distributions around the observed failure time. Figure 11b shows the temporal evolution of the predictive distribution of t_c. In late June, the predicted t_c values exhibit large variability and/or drifting behaviour. From 1 July onwards, the predictions become progressively more stabilised and begin to cluster around the observed failure time. Nevertheless, noticeable fluctuations persist throughout the analysis, highlighting the intrinsic variability of the LPPLS predictions under rapidly evolving conditions, particularly near the failure.

Results from other radar points in the upper portion (Fig. S8) show a broadly consistent behaviour, with large variability and drifting at early stages followed by progressive stabilisation and clustering of the predicted t_c values as failure is approached. Additional diagnosis (Fig. S9) further show that the critical exponent m remains below 1 in the final stage prior to failure, while other measures of predictive performance exhibit intermittent variability with a tendency towards reduced uncertainty and partial convergence as failure is approached.

Figure 12 displays the temporal evolution of the velocity b-value state, the dragon-king p-value state, the LPPLS state, and the resulting warning level for the Stampa rock slope. The b-value transitions from State 0 to State 1 in mid-June 2023 and further to State 2 around 20 June, remaining at this level until failure. In contrast, the dragon-king p-value remains in State 0 for most of the observation period and then transitions to State 1 and rapidly thereafter to State 2 on 30 June 2023. The LPPLS state remains at State 0 during most of the observation period, transitions to State 1 from 28 June, and further to State 2 from 29 June onwards in the final stage prior to failure. Based on these transitions, the warning level evolves from green to yellow in mid-June, remains at yellow until late June, and then escalates rapidly through orange to red on 30 June, immediately preceding the first failure event and about two days prior to the second failure event in early July 2023.

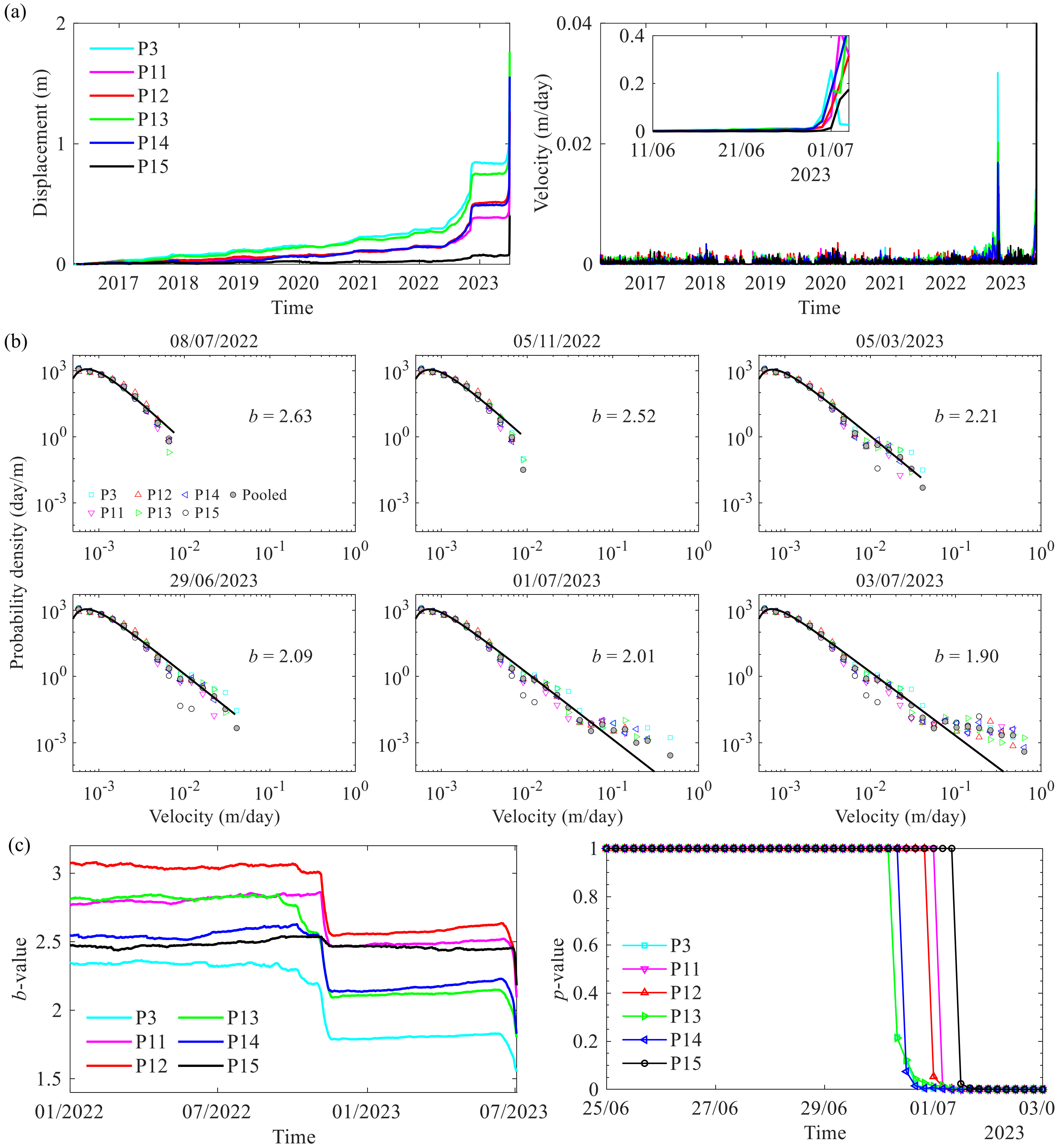

Figure 9: (a) Time series of displacement and daily velocity of the Stampa landslide, measured by seven radar points (P3 and P11–P15). (b) Probability density distributions of slope velocity at selected dates, with fitted inverse gamma distributions to the pooled data and corresponding tail exponent *b* indicated. (c) Temporal evolution of the velocity *b*-value (left) and dragon-king *p*-value (right) derived from individual radar points.

https://doi.org/10.5194/egusphere-2026-2565
Preprint. Discussion started: 20 May 2026
© Author(s) 2026. CC BY 4.0 License.

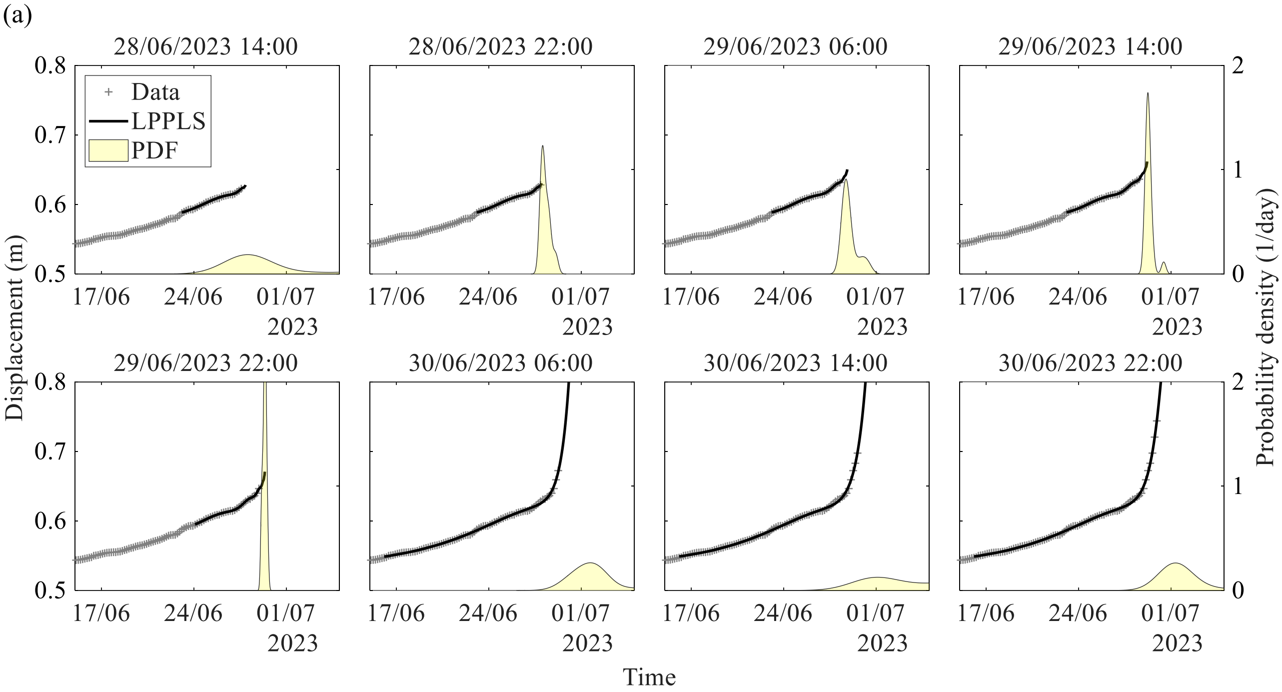

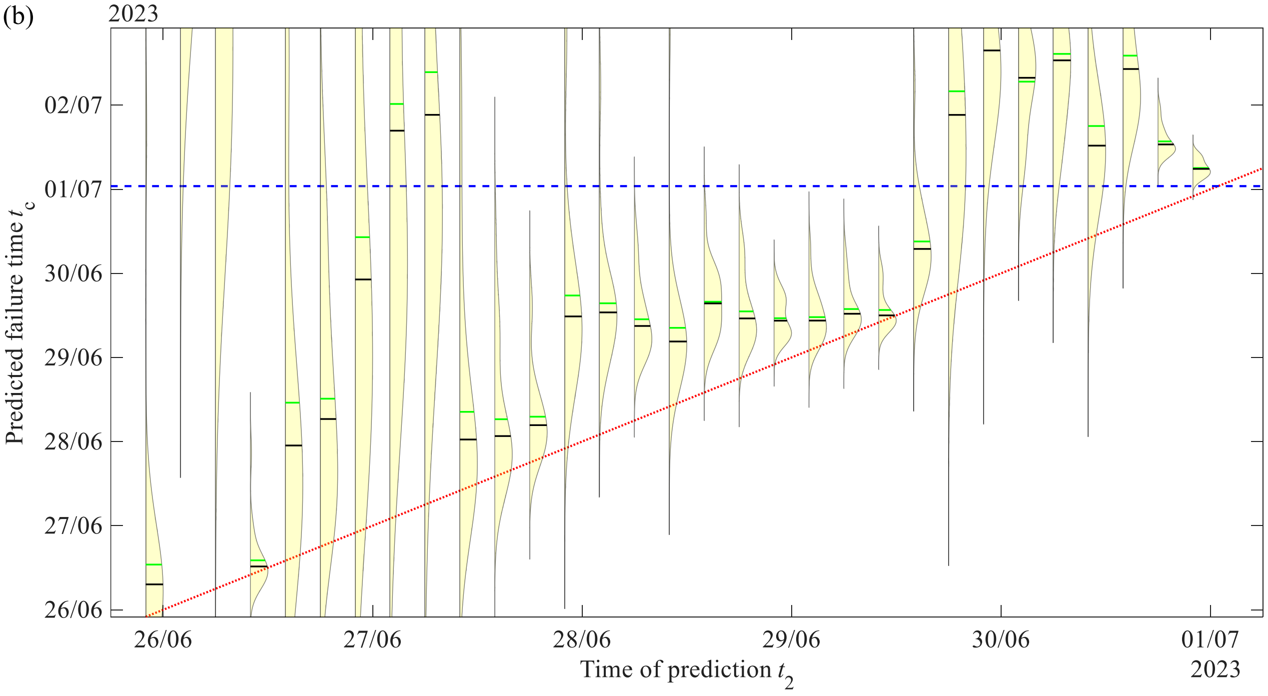

440

Figure 10: LPPLS-based time-to-failure analysis for the Stampa landslide based on radar point P3. (a) LPPLS fits to displacement data at selected times before the first failure event (01 July 2023, 00:54) and the corresponding probability density functions (PDFs) of t_c. (b) Evolution of the PDF of anticipated failure time t_c as a function of analysis time t_2, advanced at 4-hour steps. The green and black lines within each violin indicate the mean and median of the predicted t_c distribution. The red dotted line indicates the reference line $t_c = t_2$, while the blue dashed line marks the observed first failure event. 445

https://doi.org/10.5194/egusphere-2026-2565
Preprint. Discussion started: 20 May 2026
© Author(s) 2026. CC BY 4.0 License.

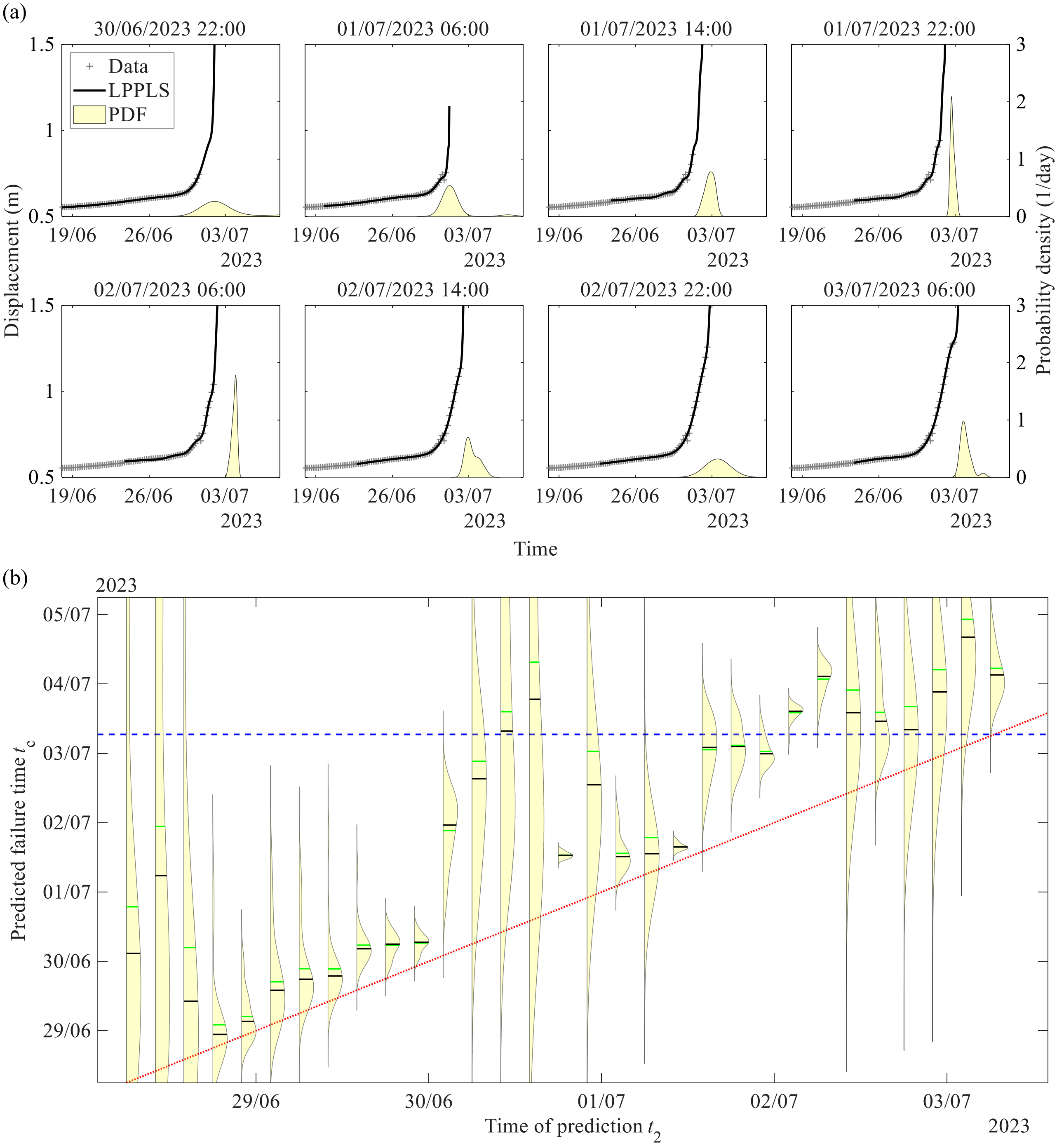

Figure 11: LPPLS-based time-to-failure analysis for the Stampa landslide based on radar point P12. (a) LPPLS fits to displacement data at selected times before the second failure event (03 July 2023, 06:33) and the corresponding probability density functions (PDFs) of t_c. (b) Evolution of the PDF of anticipated failure time t_c as a function of analysis time t_2, advanced at 4-hour 450 steps. The green and black lines within each violin indicate the mean and median of the predicted t_c distribution. The red dotted line indicates the reference line $t_c = t_2$, while the blue dashed line marks the observed second failure event.

© Author(s) 2026. CC BY 4.0 License.

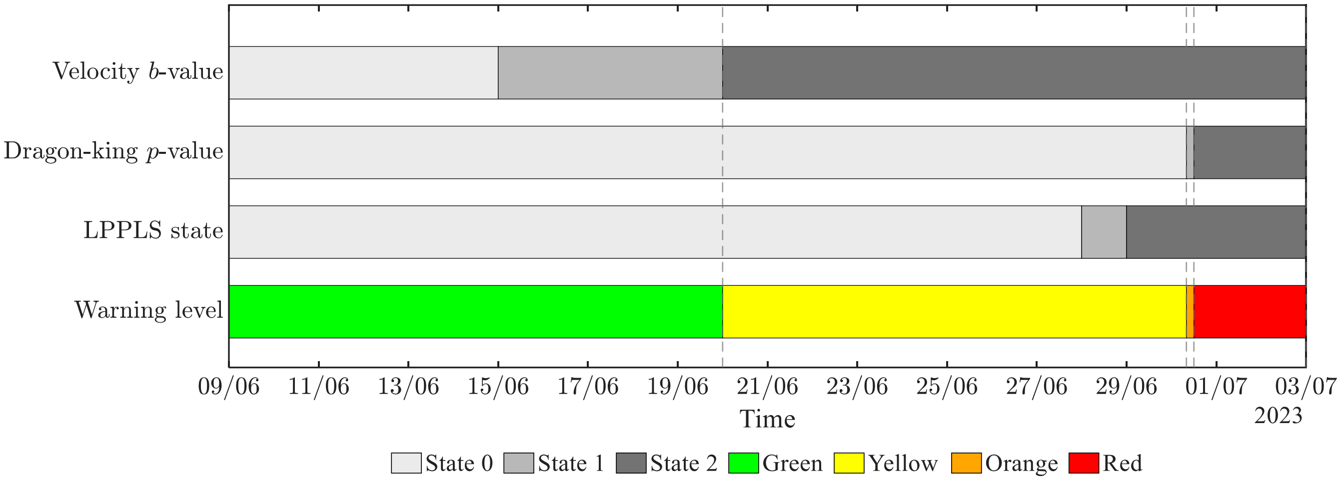

Figure 12: Temporal evolution of indicator states of velocity *b*-value, dragon-king *p*-value, and LPPLS, and the resulting traffic-light warning level, for the Stampa landslide.

5 Discussion

The three statistical physics-based diagnostics proposed in this study reveal a coherent sequence of precursory signals during the evolution of catastrophic landslides. Across the Preonzo, Veslemannen and Stampa case studies, the velocity b-value began to decline months to years before failure, indicating an increasing prevalence of larger velocity events. Dragon-king detection subsequently identified statistically significant velocity outliers, marking the emergence of extreme behaviour in the days to weeks preceding collapse. Finally, LPPLS analyses provide diagnostic information on the timing of failure by revealing transient to more persistent clustering of the predicted critical time as failure is approached. These complementary indicators therefore activate at different stages of the slope failure process, providing distinct yet mutually reinforcing information on the evolving instability: the b-value offers a long-term diagnostic of the transition from secondary to tertiary creep, the dragon-king p-value supplies a short-term alert when extreme events emerge, and LPPLS analysis provides diagnostic information on failure timing and associated uncertainty. The staged multi-diagnostic traffic-light framework eventually integrates these signals, enabling decision-makers to translate complex system dynamics into intuitive warning levels.

It is important to stress that these multi-scale indicators identified and used in our framework are rooted in the underlying physical processes governing slope instability, reflecting the hierarchical organisation of damage in heterogeneous geomaterials at the site scale. In the early stage, slope deformation is dominated by diffuse damage accumulation, leading to a gradual increase in medium-to-large velocity events and a corresponding decline in the b-value, signalling initial destabilisation driven by the interplay between exogenous forcing and endogenous damage–healing processes (Lei and Sornette, 2025a). With continued damage accumulation, interactions between locally damaged regions become increasingly important, promoting positive feedback that drives the emergence of dragon-king behaviour (Sornette, 2002; Lei et al., 2023). This hierarchical organisation is further reflected in the LPPLS structure of slope displacement evolution, where oscillations superimposed on the accelerating trend mark discrete scale invariance (Sornette, 1998), a characteristic signature of hierarchical damage and rupture processes in heterogeneous systems (Johansen and Sornette, 2000; Zhou and Sornette, 2002; Lei and Sornette, 2025e, b, d, c).

This traffic-light early warning system addresses key limitations of conventional early warning approaches, which often rely on empirical thresholds and suffer from large uncertainties. One such conventional approach is based on velocity thresholds (Crosta and Agliardi, 2002, 2003; Crosta et al., 2017; Intrieri et al., 2012; Segalini et al., 2018), which may be effective in cases where slope deformation follows a monotonic acceleration towards failure, such as the Preonzo landslide (Loew et al., 2017). However, these thresholds are typically defined for specific sites based on empirical observations, resulting in limited transferability across sites (Michoud et al., 2013). Furthermore, they are sensitive to short-term fluctuations in velocity, which can often trigger false alarms, as observed for the Veslemannen landslide (Kristensen et al., 2021), and sometimes require frequent adjustment based on subjective judgement in response to evolving system dynamics. Compared to velocity thresholds, the velocity *b*-value and dragon-king *p*-value indicators used in our framework are less sensitive to short-term fluctuations, as they reflect the evolving statistical properties of the full velocity distribution rather than individual transient velocity fluctuations. Such distributional evolution also provides a more reliable indication of the progressive transition of system state towards instability and potential of regime shift. Other early warning approaches based on the tangential angle of velocity time series, essentially characterising the acceleration, have also been proposed in conjunction with empirically defined thresholds (Ju et al., 2020; Xu et al., 2011), but they similarly rely on site-specific calibration and are sensitive to variability in deformation patterns, limiting their robustness under non-monotonic accelerating conditions and their transferability across sites.

In addition, the inverse velocity method has been widely used for forecasting slope failure by extrapolating inverse velocity to estimate the time of failure (Intrieri et al., 2019; Leinauer et al., 2023), but is often associated with substantial uncertainty (Intrieri and Gigli, 2016; Loew et al., 2017, 2024; Kristensen et al., 2021). A major source of uncertainty is the intermittent nature of slope rupture processes, typically characterised by progressively shorter quiescent phases interspersed with sudden bursts of intense activity, rather than a smooth, monotonic evolution of deformation. Moreover, linear inverse velocity extrapolation is often suggested for use in practice (Carlà et al., 2017; Intrieri et al., 2019; Voight, 1988), whereas observations frequently exhibit pronounced nonlinearity, further complicating reliable failure time estimation. Furthermore, inverse velocity analysis has commonly been applied to derive point estimates of failure time, which may not adequately represent the inherent uncertainty of the system (Carlà et al., 2017; Intrieri et al., 2019; Kristensen et al., 2021; Loew et al., 2017, 2024; Voight, 1988), highlighting the need for probabilistic frameworks that characterise the plausible range of failure times. Early warning systems based on inverse velocity analysis have also been proposed (Manconi and Giordan, 2015; Carlà et al., 2017), but their performance is also limited in practice, particularly under intermittent deformation conditions. In contrast, the LPPLS model can explicitly capture nonlinear acceleration and intermittent dynamics through its log-periodic structure (Lei and Sornette, 2025b, e), enabling a more robust characterisation of the approach to failure. By adopting a probabilistic formulation based on ensembles of model calibrations, it provides a distribution of possible failure times rather than a single deterministic estimate, thereby offering a more comprehensive representation of uncertainty.

Apart from velocity-based early warning approaches, rainfall thresholds have also been widely adopted in practice (Guzzetti et al., 2007, 2020; Segoni et al., 2015; Patton et al., 2023). These thresholds are typically derived empirically from regional datasets and have proven useful for large-scale hazard assessment. However, their applicability at the scale of individual slopes remains limited (Intrieri et al., 2013). Moreover, such approaches implicitly assume that landslide response is primarily controlled by external forcing and that the system reacts in a relatively direct and efficient manner to rainfall inputs. In contrast, increasing evidence suggests that landslide dynamics—particularly in the late stage prior to failure—are strongly governed by endogenous processes, including progressive damage, stress redistribution, and internal feedback mechanisms (Lei and Sornette, 2025a, b, e). Within this perspective, external triggers may act only as perturbations to a system that is already approaching a critical state, rather than being the sole driver of failure. The indicators adopted in our framework are designed to capture this transition of the internal state of landslides, from a stable or quasi-stable condition to an increasingly unstable regime. It is important to note that the present framework is primarily intended for landslides governed by progressive damage accumulation. For failures triggered predominantly by exceptionally extreme external events, such as great earthquakes, the predictability of landslides is inherently constrained by the predictability of these external forcings.

A key strength of the proposed framework lies in the integration of multiple complementary indicators. Rather than relying on a single metric, which may be unstable or subject to high uncertainty, the framework combines b-value evolution, dragon-king detection, and LPPLS analysis in a complementary manner. This multi-indicator approach enhances robustness by capturing different aspects of the failure process across timescales, thereby reducing sensitivity to noise and spurious fluctuations, and minimising the rate of false alarms. At the same time, the convergence of independent signals increases confidence in the identification of impending failure, supporting more reliable and informed early warning decisions. Another advantage of the proposed framework is that it combines a process-based foundation grounded in statistical physics with an observation-based adaptation to the evolving dynamics of the monitored system. This dual nature allows the method to remain physically interpretable while flexibly responding to real-time monitoring data. As a result, the framework is inherently more transferable across different sites and conditions, and requires less subjective adjustment compared to conventional threshold-based early warning approaches.

While the results presented here demonstrate the potential of the proposed framework, we do not claim that it can be universally applied to all landslide scenarios. Rather, it represents a promising approach that warrants further testing and validation across diverse geological and monitoring settings. Several limitations should be acknowledged. In particular, inferred signals from LPPLS analysis exhibit significant variability and less well-defined transitions compared to those derived from the velocity b-value and dragon-king p-value indicators. This may partly reflect the numerical sensitivity of the LPPLS model near finite-time singularity, where small perturbations—including rounding effects and data noise—can lead to large variations in the inferred parameters. This highlights the need to adopt a dynamic rather than static perspective, in

© Author(s) 2026. CC BY 4.0 License.

which forecasts are continuously updated as new data become available to reflect the evolving system dynamics. Further methodological developments are underway to improve the robustness of LPPLS inference.

In addition, the performance of the proposed early warning framework depends on the placement and quality of monitoring sensors, which must be capable of capturing the evolving dynamics of the slope. This requires multidisciplinary expertise in monitoring system design, sensor deployment, and the interpretation of site-specific geological and kinematic conditions. Finally, the framework is not intended to replace existing early warning systems, but rather to complement them by providing additional, physics-informed diagnostic information. In this sense, it offers a promising pathway towards more robust and informative early warning strategies, while requiring continued validation and integration with established practices.

6 Conclusions

This study has introduced a staged multi-diagnostic traffic-light landslide early warning system that integrates velocity *b*-value tracking, dragon-king detection, and LPPLS time-to-failure analysis within a unified, physics-informed framework. The key contribution lies in combining multiple statistical diagnostics that capture complementary precursory signatures across different stages of slope evolution, from gradual destabilisation to imminent failure. Unlike traditional approaches based on empirical thresholds or single indicators, the proposed framework explicitly accounts for the intermittent, nonlinear, and heterogeneous nature of landslide dynamics, thereby overcoming key limitations associated with non-monotonic behaviour and high variability. By integrating and translating these physically grounded precursory signatures into a traffic-light system, the framework improves both robustness and interpretability, providing physically meaningful and decision-relevant insights into the evolving system state. This multi-indicator strategy enables more reliable identification of regime transitions and enhances confidence in early warning decisions, offering a scalable and transferable approach for operational applications. Overall, this work demonstrates that combining statistical physics-based diagnostics provides a powerful pathway towards more robust and informative landslide early warning.

Data availability

No new datasets were generated in this study. The analysis is based on previously published studies and datasets (Kristensen et al., 2021; Loew et al., 2017; Loew, 2024; Maschler et al., 2025, 2026). All data used to generate the figures are available from those cited sources. Readers are referred to these publications and their associated repositories or supplementary materials for access to the underlying data.

Author contributions

QL and DS conceived the study, devised the method, and interpreted the results. QL performed the analysis and wrote the manuscript. DS reviewed and edited the manuscript.

Competing interests

The authors declare that they have no conflict of interest.

Disclaimer

Copernicus Publications remains neutral with regard to jurisdictional claims made in the text, published maps, institutional affiliations, or any other geographical representation in this paper. While Copernicus Publications makes every effort to include appropriate place names, the final responsibility lies with the authors. Views expressed in the text are those of the authors and do not necessarily reflect the views of the publisher.

Acknowledgement

During manuscript preparation, the authors used ChatGPT to assist with language editing and readability. The authors reviewed and edited the manuscript and take full responsibility for its content.

Financial support

This work was supported by the European Research Council (ERC Consolidator Grant, grant no. 101232311) and the Norwegian Water Resources and Energy Directorate. The research was also partially supported by the National Natural Science Foundation of China (Grant No. U2039202, T2350710802) and the Shenzhen Science and Technology Innovation Commission (Grant No. GJHZ20210705141805017).

References

Carlà, T., Intrieri, E., Di Traglia, F., Nolesini, T., Gigli, G., and Casagli, N.: Guidelines on the use of inverse velocity method as a tool for setting alarm thresholds and forecasting landslides and structure collapses, Landslides, 14, 517–534, https://doi.org/10.1007/s10346-016-0731-5, 2017.

Chernick, M. R.: Bootstrap Methods: A Guide for Practitioners and Researchers, John Wiley & Sons, Hoboken, 2011.

Cranmer, K.: Kernel estimation in high-energy physics, Computer Physics Communications, 136, 198–207, https://doi.org/10.1016/S0010-4655(00)00243-5, 2001.

© Author(s) 2026. CC BY 4.0 License.

Crosta, G. B. and Agliardi, F.: How to obtain alert velocity thresholds for large rockslides, Phys. Chem. Earth, 27, 1557–1565, https://doi.org/10.1016/S1474-7065(02)00177-8, 2002.

Crosta, G. B. and Agliardi, F.: Failure forecast for large rock slides by surface displacement measurements, Can. Geotech. J., 40, 176–191, https://doi.org/10.1139/t02-085, 2003.

Crosta, G. B., Agliardi, F., Rivolta, C., Alberti, S., and Dei Cas, L.: Long-term evolution and early warning strategies for complex rockslides by real-time monitoring, Landslides, 14, 1615–1632, https://doi.org/10.1007/s10346-017-0817-8, 2017.

Demos, G. and Sornette, D.: Comparing nested data sets and objectively determining financial bubbles' inceptions, Physica A Stat. Mech. Appl., 524, 661–675, https://doi.org/10.1016/j.physa.2019.04.050, 2019.

Filimonov, V. and Sornette, D.: A stable and robust calibration scheme of the log-periodic power law model, Physica A Stat. Mech. Appl., 392, 3698–3707, https://doi.org/10.1016/j.physa.2013.04.012, 2013.

Froude, M. J. and Petley, D. N.: Global fatal landslide occurrence from 2004 to 2016, Nat. Hazards Earth Syst. Sci., 18, 2161–2181, https://doi.org/10.5194/nhess-18-2161-2018, 2018.

Gariano, S. L. and Guzzetti, F.: Landslides in a changing climate, Earth-Sci. Rev., 162, 227–252, https://doi.org/10.1016/j.earscirev.2016.08.011, 2016.

Gschwind, S., Loew, S., and Wolter, A.: Multi-stage structural and kinematic analysis of a retrogressive rock slope instability complex (Preonzo, Switzerland), Eng. Geol., 252, 27–42, https://doi.org/10.1016/j.enggeo.2019.02.018, 2019.

Guzzetti, F., Peruccacci, S., Rossi, M., and Stark, C. P.: Rainfall thresholds for the initiation of landslides in central and southern Europe, Meteorol. Atmos. Phys., 98, 239–267, https://doi.org/10.1007/s00703-007-0262-7, 2007.

Guzzetti, F., Gariano, S. L., Peruccacci, S., Brunetti, M. T., Marchesini, I., Rossi, M., and Melillo, M.: Geographical landslide early warning systems, Earth-Science Reviews, 200, 102973, https://doi.org/10.1016/j.earscirev.2019.102973, 2020.

Intrieri, E. and Gigli, G.: Landslide forecasting and factors influencing predictability, Nat. Hazards Earth Syst. Sci., 16, 2501–2510, https://doi.org/10.5194/nhess-16-2501-2016, 2016.

Intrieri, E., Gigli, G., Mugnai, F., Fanti, R., and Casagli, N.: Design and implementation of a landslide early warning system, Engineering Geology, 147–148, 124–136, https://doi.org/10.1016/j.enggeo.2012.07.017, 2012.

Intrieri, E., Gigli, G., Casagli, N., and Nadim, F.: Landslide early warning system: Toolbox and general concepts, Nat. Hazards Earth Syst. Sci., 13, 85–90, https://doi.org/10.5194/nhess-13-85-2013, 2013.

Intrieri, E., Carlà, T., and Gigli, G.: Forecasting the time of failure of landslides at slope-scale: A literature review, Earth-Sci. Rev., 193, 333–349, https://doi.org/10.1016/j.earscirev.2019.03.019, 2019.

Jacquemart, M., Weber, S., Chiarle, M., Chmiel, M., Cicoira, A., Corona, C., Eckert, N., Gaume, J., Giacona, F., Hirschberg, J., Kaitna, R., Magnin, F., Mayer, S., Moos, C., Van Herwijnen, A., and Stoffel, M.: Detecting the impact of climate change on alpine mass movements in observational records from the European Alps, Earth-Science Reviews, 258, 104886, https://doi.org/10.1016/j.earscirev.2024.104886, 2024.

Johansen, A. and Sornette, D.: Critical ruptures, Eur. Phys. J. B, 18, 163–181, https://doi.org/10.1007/s100510070089, 2000.

© Author(s) 2026. CC BY 4.0 License.

Ju, N., Huang, J., He, C., Van Asch, T. W. J., Huang, R., Fan, X., Xu, Q., Xiao, Y., and Wang, J.: Landslide early warning, case studies from Southwest China, Engineering Geology, 279, 105917, https://doi.org/10.1016/j.enggeo.2020.105917, 2020.

Kristensen, L., Czekirda, J., Penna, I., Etzelmüller, B., Nicolet, P., Pullarello, J. S., Blikra, L. H., Skrede, I., Oldani, S., and Abellan, A.: Movements, failure and climatic control of the Veslemannen rockslide, Western Norway, Landslides, 18, 1963–1980, https://doi.org/10.1007/s10346-020-01609-x, 2021.

Krøgli, I. K., Devoli, G., Colleuille, H., Boje, S., Sund, M., and Engen, I. K.: The Norwegian forecasting and warning service for rainfall- and snowmelt-induced landslides, Nat. Hazards Earth Syst. Sci., 18, 1427–1450, https://doi.org/10.5194/nhess-18-1427-2018, 2018.

Lacroix, P., Handwerger, A. L., and Bièvre, G.: Life and death of slow-moving landslides, Nat. Rev. Earth Environ., 1, 404–419, https://doi.org/10.1038/s43017-020-0072-8, 2020.

Lei, Q. and Sornette, D.: A stochastic dynamical model of slope creep and failure, Geophys. Res. Lett., 50, e2022GL102587, https://doi.org/10.1029/2022GL102587, 2023.

Lei, Q. and Sornette, D.: Endo-exo framework for a unifying classification of episodic landslide movements: Implications for forecasting catastrophic failures, Sci. Adv., 11, eady9141, https://doi.org/10.1126/sciadv.ady9141, 2025a.

Lei, Q. and Sornette, D.: Log-periodic power law singularities in landslide dynamics: Statistical evidence from 52 crises, Geophysical Research Letters, 52, e2025GL116379, https://doi.org/10.1029/2025GL116379, 2025b.

Lei, Q. and Sornette, D.: Log-periodic signatures prior to volcanic eruptions: evidence from 34 events, Earth and Planetary Science Letters, 666, 119496, https://doi.org/10.1016/j.epsl.2025.119496, 2025c.

Lei, Q. and Sornette, D.: Oscillatory finite-time singularities in rockbursts, Int. J. Rock Mech. Min. Sci., 192, 106156, https://doi.org/10.1016/j.ijrmms.2025.106156, 2025d.

Lei, Q. and Sornette, D.: Unified failure model for landslides, rockbursts, glaciers, and volcanoes., Commun. Earth Environ, 6, 390, https://doi.org/10.1038/s43247-025-02369-z, 2025e.

Lei, Q., Sornette, D., Yang, H., and Loew, S.: Real-time forecast of catastrophic landslides via dragon-king detection, Geophys. Res. Lett., 50, e2022GL100832, https://doi.org/10.1029/2022GL100832, 2023.

Leinauer, J., Weber, S., Cicoira, A., Beutel, J., and Krautblatter, M.: An approach for prospective forecasting of rock slope failure time, Commun. Earth Environ., 4, 253, https://doi.org/10.1038/s43247-023-00909-z, 2023.

Loew, S.: Preonzo Rockslide Complex Displacement Data, https://doi.org/10.3929/ETHZ-B-000611239, 2024.

Loew, S., Gschwind, S., Gischig, V., Keller-Signer, A., and Valenti, G.: Monitoring and early warning of the 2012 Preonzo catastrophic rockslope failure, Landslides, 14, 141–154, https://doi.org/10.1007/s10346-016-0701-y, 2017.

Loew, S., Schneider, S., Josuran, M., Figi, D., Thoeny, R., Huwiler, A., Largiadèr, A., and Naenni, C.: Early warning and dynamics of compound rockslides: lessons learnt from the Brienz/Brinzauls 2023 rockslope failure, Landslides, 22, 283–298, https://doi.org/10.1007/s10346-024-02380-z, 2024.

Magnin, F., Etzelmüller, B., Westermann, S., Isaksen, K., Hilger, P., and Hermanns, R. L.: Permafrost distribution in steep rock slopes in Norway: measurements, statistical modelling and implications for geomorphological processes, Earth Surf. Dynam., 7, 1019–1040, https://doi.org/10.5194/esurf-7-1019-2019, 2019.

Malevergne, Y. and Sornette, D.: Extreme Financial Risks: From Dependence to Risk Management, Springer, Berlin/Heidelberg, https://doi.org/10.1007/b138841, 2006.

Manconi, A. and Giordan, D.: Landslide early warning based on failure forecast models: the example of the Mt. de La Saxe rockslide, northern Italy, Nat. Hazards Earth Syst. Sci., 15, 1639–1644, https://doi.org/10.5194/nhess-15-1639-2015, 2015.

Maschler, A., Snook, P., Schild, L., Samnøy, S. F., Kristensen, L., Dahle, H., Aalbu, J. H., Henriksen, H., Nerhus, S. D., and Scheiber, T.: Data for: Multistage 54,000 m3 Rockfall (Stampa, Western Norway): Insights from Comprehensive Monitoring and Failure Analysis (1.0), https://doi.org/10.18710/GBDO4X, 2025.

Maschler, A., Snook, P., Schild, L., Samnøy, S. F., Kristensen, L., Dahle, H., Aalbu, J. H., Henriksen, H., Nerhus, S. D., and Scheiber, T.: Multistage 54,000 m3 rockfall (Stampa, Western Norway): Insights from comprehensive monitoring and failure analysis, Landslides, 23, 851–869, https://doi.org/10.1007/s10346-025-02620-w, 2026.

Michoud, C., Bazin, S., Blikra, L. H., Derron, M.-H., and Jaboyedoff, M.: Experiences from site-specific landslide early warning systems, Nat. Hazards Earth Syst. Sci., 13, 2659–2673, https://doi.org/10.5194/nhess-13-2659-2013, 2013.

Patton, A. I., Luna, L. V., Roering, J. J., Jacobs, A., Korup, O., and Mirus, B. B.: Landslide initiation thresholds in data-sparse regions: application to landslide early warning criteria in Sitka, Alaska, USA, Nat. Hazards Earth Syst. Sci., 23, 3261–3284, https://doi.org/10.5194/nhess-23-3261-2023, 2023.

Petley, D.: Global patterns of loss of life from landslides, Geology, 40, 927–930, https://doi.org/10.1130/G33217.1, 2012.

Saleur, H., Sammis, C. G., and Sornette, D.: Discrete scale invariance, complex fractal dimensions, and log-periodic fluctuations in seismicity, J. Geophys. Res., 101, 17661–17677, https://doi.org/10.1029/96JB00876, 1996.

Schild, L., Scheiber, T., Snook, P., Arghandeh, R., Samnøy, S. F., Maschler, A., and Kristensen, L.: Multimodal Asynchronous Kalman Filter for monitoring unstable rock slopes, Geomatics, Natural Hazards and Risk, 14, 2272575, https://doi.org/10.1080/19475705.2023.2272575, 2023.

Segalini, A., Valletta, A., and Carri, A.: Landslide time-of-failure forecast and alert threshold assessment: A generalized criterion, Engineering Geology, 245, 72–80, https://doi.org/10.1016/j.enggeo.2018.08.003, 2018.

Segoni, S., Battistini, A., Rossi, G., Rosi, A., Lagomarsino, D., Catani, F., Moretti, S., and Casagli, N.: Technical Note: An operational landslide early warning system at regional scale based on space–time-variable rainfall thresholds, Nat. Hazards Earth Syst. Sci., 15, 853–861, https://doi.org/10.5194/nhess-15-853-2015, 2015.

Sornette, D.: Discrete-scale invariance and complex dimensions, Phys. Rep., 297, 239–270, https://doi.org/10.1016/S0370-1573(97)00076-8, 1998.

Sornette, D.: Predictability of catastrophic events: Material rupture, earthquakes, turbulence, financial crashes, and human birth, Proc. Natl. Acad. Sci., 99, 2522–2529, https://doi.org/10.1073/pnas.022581999, 2002.

Sornette, D. and Ouillon, G.: Dragon-kings: Mechanisms, statistical methods and empirical evidence, Eur. Phys. J. Spec. Top., 205, 1–26, https://doi.org/10.1140/epjst/e2012-01559-5, 2012.

Sornette, D. and Sammis, C. G.: Complex critical exponents from renormalization group theory of earthquakes: Implications for earthquake predictions, J. Phys. I France, 5, 607–619, https://doi.org/10.1051/jp1:1995154, 1995.

Sornette, D. and Wei, R.: Multiple outlier detection in samples with exponential & Pareto tails, Journal of Applied Statistics, 53, 224–256, https://doi.org/10.1080/02664763.2025.2511934, 2026.

Voight, B.: A method for prediction of volcanic eruptions, Nature, 332, 125–130, https://doi.org/10.1038/332125a0, 1988.

Xu, Q., Yuan, Y., Zeng, Y., and Hack, R.: Some new pre-warning criteria for creep slope failure, Sci. China Technol. Sci., 54, 210–220, https://doi.org/10.1007/s11431-011-4640-5, 2011.

Zhou, W.-X. and Sornette, D.: Generalized q analysis of log-periodicity: Applications to critical ruptures, Phys. Rev. E, 66, 046111, https://doi.org/10.1103/PhysRevE.66.046111, 2002.